



<b>Publication Year</b>	2017
<b>Acceptance in OA</b>	2020-08-27T14:05:11Z
<b>Title</b>	The NuSTAR Extragalactic Survey: Average Broadband X-Ray Spectral Properties of the NuSTAR-detected AGNs
<b>Authors</b>	Del Moro, A., Alexander, D. M., Aird, J. A., Bauer, F. E., Civano, F., Mullaney, J. R., Ballantyne, D. R., Brandt, W. N., COMASTRI, Andrea, Gandhi, P., Harrison, F. A., Lansbury, G. B., Lanz, L., Luo, B., MARCHESI, STEFANO, Puccetti, S., Ricci, C., Saez, C., Stern, D., Treister, E., ZAPPACOSTA, Luca
<b>Publisher's version (DOI)</b>	10.3847/1538-4357/aa9115
<b>Handle</b>	<a href="http://hdl.handle.net/20.500.12386/26893">http://hdl.handle.net/20.500.12386/26893</a>
<b>Journal</b>	THE ASTROPHYSICAL JOURNAL
<b>Volume</b>	849



# The *NuSTAR* Extragalactic Survey: Average Broadband X-Ray Spectral Properties of the *NuSTAR*-detected AGNs

A. Del Moro<sup>1,2</sup>, D. M. Alexander<sup>2</sup>, J. A. Aird<sup>3</sup>, F. E. Bauer<sup>4,5,6</sup>, F. Civano<sup>7,8</sup>, J. R. Mullaney<sup>9</sup>, D. R. Ballantyne<sup>10</sup>, W. N. Brandt<sup>11,12,13</sup>, A. Comastri<sup>14</sup>, P. Gandhi<sup>15</sup>, F. A. Harrison<sup>16</sup>, G. B. Lansbury<sup>2,3</sup>, L. Lanz<sup>7</sup>, B. Luo<sup>17</sup>, S. Marchesi<sup>18</sup>, S. Puccetti<sup>19,20</sup>, C. Ricci<sup>4,21,22</sup>, C. Saez<sup>23</sup>, D. Stern<sup>24</sup>, E. Treister<sup>4</sup>, and L. Zappacosta<sup>19</sup>

<sup>1</sup>Max-Planck-Institut für Extraterrestrische Physik (MPE), Giessenbachstrasse 1, D-85748 Garching, Germany; [adelmoro@mpe.mpg.de](mailto:adelmoro@mpe.mpg.de)

<sup>2</sup>Centre for Extragalactic Astronomy, Department of Physics, Durham University, South Road, Durham, DH1 3LE, UK

<sup>3</sup>Institute of Astronomy, University of Cambridge, Madingley Road, Cambridge, CB3 0HA, UK

<sup>4</sup>Instituto de Astrofísica and Centro de Astroingeniería, Facultad de Física, Pontificia Universidad Católica de Chile, Casilla 306, Santiago 22, Chile

<sup>5</sup>Millennium Institute of Astrophysics (MAS), Nuncio Monseñor Sótero Sanz 100, Providencia, Santiago, Chile

<sup>6</sup>Space Science Institute, 4750 Walnut Street, Suite 205, Boulder, CO 80301, USA

<sup>7</sup>Department of Physics and Astronomy, Dartmouth College, 6127 Wilder Laboratory, Hanover, NH 03755, USA

<sup>8</sup>Harvard-Smithsonian Center for Astrophysics, 60 Garden Street, Cambridge, MA 02138, USA

<sup>9</sup>Department of Physics & Astronomy, University of Sheffield, Sheffield, S3 7RH, UK

<sup>10</sup>Center for Relativistic Astrophysics, School of Physics, Georgia Institute of Technology, Atlanta, GA 30332, USA

<sup>11</sup>Department of Astronomy and Astrophysics, 525 Davey Lab, The Pennsylvania State University, University Park, PA 16802, USA

<sup>12</sup>Institute for Gravitation and the Cosmos, The Pennsylvania State University, University Park, PA 16802, USA

<sup>13</sup>Department of Physics, 104 Davey Lab, The Pennsylvania State University, University Park, PA 16802, USA

<sup>14</sup>INAF—Osservatorio Astronomico di Bologna, via Gobetti 93/3, I-40129 Bologna, Italy

<sup>15</sup>Department of Physics & Astronomy, Faculty of Physical Sciences and Engineering, University of Southampton, Southampton, SO17 1BJ, UK

<sup>16</sup>Cahill Center for Astrophysics, 1216 East California Boulevard, California Institute of Technology, Pasadena, CA 91125, USA

<sup>17</sup>School of Astronomy and Space Science, Nanjing University, Nanjing 210093, China

<sup>18</sup>Department of Physics & Astronomy, Clemson University, Clemson, SC 29634, USA

<sup>19</sup>INAF—Osservatorio Astronomico di Roma, via Frascati 33, I-00040 Monteporzio Catone, Italy

<sup>20</sup>Agenzia Spaziale Italiana—Unità di Ricerca Scientifica, Via del Politecnico, 00133 Roma, Italy

<sup>21</sup>EMBIGGEN Anillo, Concepcion, Chile

<sup>22</sup>Kavli Institute for Astronomy and Astrophysics, Peking University, Beijing 100871, China

<sup>23</sup>Osservatorio Astronomico Cerro Calán, Departamento de Astronomía, Universidad de Chile, Casilla 36-D, Santiago, Chile

<sup>24</sup>Jet Propulsion Laboratory, California Institute of Technology, 4800 Oak Grove Drive, Mail Stop 169-221, Pasadena, CA 91109, USA

Received 2017 February 6; revised 2017 September 26; accepted 2017 October 2; published 2017 October 31

## Abstract

We present a study of the average X-ray spectral properties of the sources detected by the *NuSTAR* extragalactic survey, comprising observations of the Extended Chandra Deep Field South (E-CDFS), Extended Groth Strip (EGS), and the Cosmic Evolution Survey (COSMOS). The sample includes 182 *NuSTAR* sources (64 detected at 8–24 keV), with 3–24 keV fluxes ranging between  $f_{3-24 \text{ keV}} \approx 10^{-14}$  and  $6 \times 10^{-13} \text{ erg cm}^{-2} \text{ s}^{-1}$  ( $f_{8-24 \text{ keV}} \approx 3 \times 10^{-14}$ – $3 \times 10^{-13} \text{ erg cm}^{-2} \text{ s}^{-1}$ ) and redshifts in the range of  $z = 0.04$ – $3.21$ . We produce composite spectra from the *Chandra* + *NuSTAR* data ( $E \approx 2$ – $40 \text{ keV}$ , rest frame) for all the sources with redshift identifications (95%) and investigate the intrinsic, average spectra of the sources, divided into broad-line (BL) and narrow-line (NL) active galactic nuclei (AGNs), and also in different bins of X-ray column density and luminosity. The average power-law photon index for the whole sample is  $\Gamma = 1.65_{-0.03}^{+0.03}$ , flatter than the  $\Gamma \approx 1.8$  typically found for AGNs. While the spectral slope of BL and X-ray unabsorbed AGNs is consistent with the typical values ( $\Gamma = 1.79_{-0.01}^{+0.01}$ ), a significant flattening is seen in NL AGNs and heavily absorbed sources ( $\Gamma = 1.60_{-0.05}^{+0.08}$  and  $\Gamma = 1.38_{-0.12}^{+0.12}$ , respectively), likely due to the effect of absorption and to the contribution from the Compton reflection component to the high-energy flux ( $E > 10 \text{ keV}$ ). We find that the typical reflection fraction in our spectra is  $R \approx 0.5$  (for  $\Gamma = 1.8$ ), with a tentative indication of an increase of the reflection strength with X-ray column density. While there is no significant evidence for a dependence of the photon index on X-ray luminosity in our sample, we find that  $R$  decreases with luminosity, with relatively high levels of reflection ( $R \approx 1.2$ ) for  $L_{10-40 \text{ keV}} < 10^{44} \text{ erg s}^{-1}$  and  $R \approx 0.3$  for  $L_{10-40 \text{ keV}} > 10^{44} \text{ erg s}^{-1}$  AGNs, assuming a fixed spectral slope of  $\Gamma = 1.8$ .

**Key words:** galaxies: active – quasars: general – surveys – X-rays: galaxies

## 1. Introduction

Studies of the cosmic X-ray background (CXB) have demonstrated that the diffuse X-ray emission observed as a background radiation in X-ray surveys can be explained by the summed emission from unresolved X-ray sources, mainly active galactic nuclei (AGNs) at low and high redshift. Moreover, the majority of these AGNs must be obscured to reproduce the characteristic CXB spectrum peak at  $E \approx 20$ – $30 \text{ keV}$  (Comastri et al. 1995; Treister & Urry 2005;

Gilli et al. 2007; Ballantyne 2009; Treister et al. 2009). In particular, synthesis models of the CXB require a population of heavily obscured AGNs, defined as Compton thick (CT), where the equivalent hydrogen column density ( $N_{\text{H}}$ ) exceeds the inverse of the Thomson scattering cross section ( $N_{\text{H}} > 1/\sigma_{\text{T}} \approx 1.5 \times 10^{24} \text{ cm}^{-2}$ ). The fraction of such sources and their space density, however, are still uncertain and vary from model to model, depending on different parameter assumptions ( $\sim 10\%$ – $30\%$ ; e.g., Gilli et al. 2007; Treister

et al. 2009; Akylas et al. 2012). The main differences between these models reside in the adopted  $N_{\text{H}}$  distribution of the AGN population, the X-ray luminosity function (XLF), and the AGN spectral models. Many of these parameters are degenerate, and this prevents us from securely determining the composition of the CXB at its peak (e.g., Treister et al. 2009; Akylas et al. 2012).

At energies  $E < 10$  keV the sensitive surveys undertaken with *Chandra* and *XMM-Newton* have allowed us to resolve directly up to 90% of the CXB as individual sources, placing important constraints on the total AGN population (Hickox & Markevitch 2006; Xue et al. 2012). However, even these surveys struggle to detect and identify the most-obscured AGNs, or tend to underestimate the intrinsic column density of these sources (e.g., Del Moro et al. 2014; Lansbury et al. 2014; Lansbury et al. 2015), especially at high redshift, leaving significant uncertainties on the intrinsic  $N_{\text{H}}$  distribution. Moreover, the lack of direct sensitive measurements of the AGN population at high energies ( $E \gtrsim 10$  keV), due to the lack of sensitive hard X-ray telescopes until the past few years, has only allowed us to resolve directly  $\sim 1\%$ – $2\%$  of the CXB at its peak (e.g., with *Swift*-BAT or *INTEGRAL*; Krivonos et al. 2007; Ajello et al. 2008; Bottacini et al. 2012). Therefore, our knowledge and models of the CXB composition at high energies solely rely on extrapolations from lower energies.

The extragalactic survey program undertaken by *NuSTAR*, the first sensitive hard X-ray telescope ( $E \approx 3$ – $79$  keV) with focusing optics (Harrison et al. 2013), provides great improvements on our understanding of the AGN population at  $E > 10$  keV. With the sources detected by *NuSTAR* in the Extended Chandra Deep Field South (E-CDFS; Mullaney et al. 2015), Cosmic Evolution Survey (COSMOS; Civano et al. 2015), Extended Groth Strip (EGS; A. Del Moro et al. 2017, in preparation), and the serendipitous survey fields (Alexander et al. 2013; Lansbury et al. 2017), we are now able to resolve directly  $\approx 35\%$  of the CXB at  $E = 8$ – $24$  keV (Harrison et al. 2016), a much higher fraction than possible with pre-*NuSTAR* telescopes. However, the first studies of the XLF with *NuSTAR* (Aird et al. 2015a) have shown that there are still degeneracies in the models to reconcile the XLF derived from *NuSTAR* sources with extrapolations from the lower-energy (2–10 keV) XLFs, in particular related to the distribution of absorbing column densities and the intrinsic spectral properties of AGNs, such as the strength of the Compton reflection component. Detailed X-ray spectral analysis of the *NuSTAR* sources is required to break these degeneracies and place tighter constraints on the measurements of the XLF and the AGN population contributing to the CXB.

In this paper we aim to investigate the average broadband X-ray ( $\sim 0.5$ – $25$  keV) spectral properties of the *NuSTAR* sources detected in the E-CDFS, COSMOS, and EGS fields, in order to constrain the intrinsic spectral properties of the sources and measure the typical strength of the Compton reflection. To this end we produce rest-frame composite spectra at  $\sim 2$ – $40$  keV (rest frame) with *Chandra*+*NuSTAR* data for the whole sample and for various subsamples, to investigate how the spectral parameters might vary between broad-line (BL) and narrow-line (NL) AGNs, or as a function of X-ray column density and luminosity. A study focusing on the spectral analysis of the brightest hard-band (HB; 8–24 keV) detected sources is presented in a companion paper (L. Zappacosta et al. 2017, in preparation).

**Table 1**  
*NuSTAR* Source Sample Summary

Field	No. of Sources	HB <sup>a</sup>	Redshift <sup>b</sup>	BL AGNs	NL AGNs
E-CDFS	49	19	45 (42)	18 (18)	19 (19)
EGS	42	13	42 (33)	18 (18)	21 (14)
COSMOS	91	32	86 (80)	40 (40)	29 (29)
Total	182	64	173 (155)	76 (76)	69 (62)

**Notes.**

<sup>a</sup> Number of HB (8–24 keV) detected sources.

<sup>b</sup> Including both spectroscopic and photometric redshifts; the number of spectroscopic redshifts is reported in parentheses (also in the fifth and sixth columns).

Throughout the paper we assume a cosmological model with  $H_0 = 70$  km s<sup>-1</sup> Mpc<sup>-1</sup>,  $\Omega_M = 0.27$ , and  $\Omega_\Lambda = 0.73$  (Spergel et al. 2003). All the errors and upper limits are quoted at a 90% confidence level, unless otherwise specified.

## 2. Data and Catalogs

The *NuSTAR* extragalactic survey program consists of tiered observations of well-known survey fields: (i) a set of deep tiled pointings covering the E-CDFS (Mullaney et al. 2015) and EGS (A. Del Moro et al. 2017, in preparation) fields, with an area of  $\approx 30 \times 30$  and  $\approx 12 \times 54$  arcmin<sup>2</sup>, respectively, and a total exposure of 1.49 Ms in each of the two fields, reaching a maximum exposure of  $\approx 220$  ks in E-CDFS and  $\approx 280$  ks in EGS (at 3–24 keV in each focal plane module (FPM), vignetting corrected); (ii) a medium-depth set of 121 tiled pointings covering  $\approx 1.7$  deg<sup>2</sup> of the COSMOS field (Civano et al. 2015) for a total exposure of 3.12 Ms, with a maximum depth of  $\approx 90$  ks in the central  $\sim 1.2$  deg<sup>2</sup>; (iii) a serendipitous survey consisting of all serendipitous sources detected in any *NuSTAR* targeted observation (excluding all sources associated with the target; Alexander et al. 2013; Lansbury et al. 2017). This last tier of the survey spans a wide range of depths (see, e.g., Aird et al. 2015a; Lansbury et al. 2017) and has the largest sky coverage, reaching  $\approx 13$  deg<sup>2</sup> to date (still ongoing).

Since in this work we require low-energy ( $E < 10$  keV) *Chandra* data, together with the *NuSTAR* data, to produce broad X-ray band composite spectra, we limit our analyses to the sources detected in the E-CDFS, EGS, and COSMOS fields, which have good *Chandra* coverage and redshift completeness (spectroscopic and photometric), while we exclude the serendipitous survey sources owing to the heterogeneity of the available ancillary data. Although *XMM-Newton* observations are also available for the E-CDFS and COSMOS fields, we do not include these data in our analyses because combining the data from different X-ray instruments to produce the composite spectra can cause significant distortions in the resulting spectra (see Section 3.2.1). Our sample consists of 182 AGNs (see Table 1), 49 detected in E-CDFS (Mullaney et al. 2015), 42 detected in EGS (A. Del Moro et al. 2017, in preparation), and 91 detected in COSMOS (Civano et al. 2015). Of these sources, 64 ( $\sim 35\%$ ) are detected in the *NuSTAR* HB (8–24 keV).<sup>25</sup>

<sup>25</sup> Most of the sources that are formally HB undetected ( $\sim 65\%$ ) are actually detected also above 8 keV, but with lower significance than the false-probability threshold adopted by Civano et al. (2015), Mullaney et al. (2015), and A. Del Moro et al. (2017, in preparation).

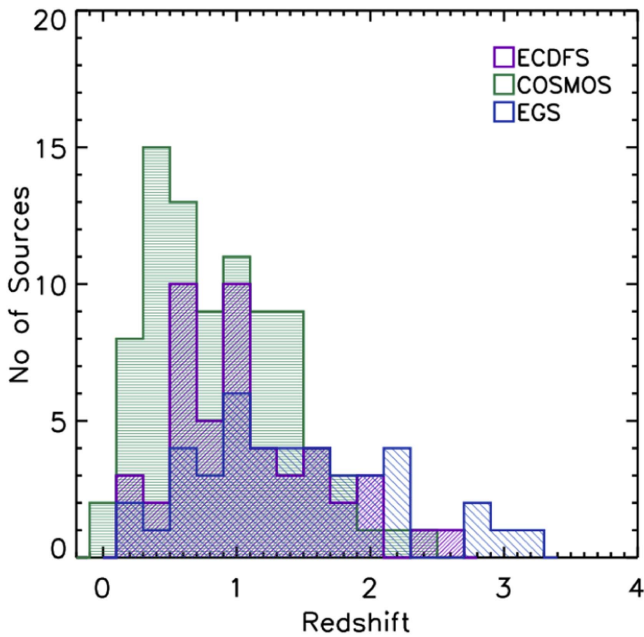


**Figure 1.** Redshift distribution for the sources detected in the various survey fields: E-CDFS (magenta), EGS (blue), COSMOS (green). The redshift distribution is in the range  $z = 0.044$ – $3.215$ , with a mean redshift  $\langle z \rangle \approx 1.065$  (median  $z \approx 1.021$ ).

In Civano et al. (2015) and Mullaney et al. (2015), the *NuSTAR* sources have been matched to the *Chandra* and/or *XMM-Newton* point-source catalogs available in these fields (Lehmer et al. 2005; Brusa et al. 2010; Xue et al. 2011; Ranalli et al. 2013; Nandra et al. 2015; Civano et al. 2016; Marchesi et al. 2016) using a nearest-neighbor approach with a matching radius of  $30''$ , to identify a lower X-ray energy counterpart and thus obtain the multiwavelength information, such as the spectroscopic or photometric redshift and optical classification. The same approach has been used for the sources in the EGS field (A. Del Moro et al., in preparation). A total of 11 out of 49 ( $\sim 22\%$ ) sources in E-CDFS, 14 out of 91 sources ( $\sim 15\%$ ) in COSMOS, and 10 out of 42 sources ( $\sim 24\%$ ) in EGS can be associated with multiple counterparts within the  $30''$  matching radius. In our spectral analyses we use the primary counterpart identified by Civano et al. (2015) for the COSMOS sources, while for the E-CDFS and EGS sources, for which a primary counterpart among the possible candidates has not been specified in the catalogs (see, e.g., Mullaney et al. 2015), we choose the *Chandra* counterpart that more closely matches the *NuSTAR* flux at 3–7 keV (see Section 3.1). We note that the *NuSTAR* flux for these sources could still include some contribution from the secondary counterparts; however, this contribution is expected to be limited. We estimated that the fluxes of the secondary counterparts are typically  $< 35\%$  of the *NuSTAR* flux at 3–7 keV.

With the low X-ray energy counterpart identification we also obtained the redshift and the optical class associated with those sources from existing catalogs (Brusa et al. 2010; Xue et al. 2011; Nandra et al. 2015). The redshift distribution of the *NuSTAR* sources detected in the different survey fields is shown in Figure 1. In the E-CDFS field there are 44 out of 49 redshift identifications for the *NuSTAR*-detected sources ( $\sim 90\%$ ); of these redshifts, 41 are spectroscopic ( $\sim 93\%$ ) and 3 are photometric redshifts ( $\sim 7\%$ ; see Mullaney et al. 2015). In

addition to the redshifts reported in the *NuSTAR* catalog by Mullaney et al. (2015), we include a redshift identification for *NuSTAR* J033243-2738.3 (XID 437, in Lehmer et al. 2005) of  $z \approx 1.6$ , taken from Vignali et al. (2015), which is derived directly from the *XMM* X-ray spectrum, resulting in a total of 45 redshift identifications ( $\sim 92\%$ ). In the COSMOS field 86 out of the 91 *NuSTAR* sources have a *Chandra* and/or *XMM-Newton* counterpart and redshift identification (see Civano et al. 2015), of which  $\sim 93\%$  are spectroscopic (80/86 sources) and  $\sim 7\%$  are photometric (6/86 sources), yielding the same redshift identification fractions as in the E-CDFS field. In the EGS field all 42 sources have a redshift identification; however, the fraction of spectroscopic redshifts is lower than in the other fields: 33 sources have spectroscopic identification ( $\sim 79\%$ ), while 9 have photometric redshift ( $\sim 21\%$ ). The redshifts of the whole sample span the range of  $z = 0.044$ – $3.215$ , with a mean redshift  $\langle z \rangle \approx 1.065$  (median  $z \approx 1.021$ ).

From these catalogs we also took the optical classification for our *NuSTAR* sources, where available. The classification of the sources in the E-CDFS and COSMOS fields comes from optical spectroscopy: 18 and 40 sources are classified as BL AGNs (FWHM  $> 2000 \text{ km s}^{-1}$ ) and 19 and 29 as NL AGNs or emission-line galaxies (included in this paper as “NL AGNs”) in E-CDFS and COSMOS, respectively (see Table 1). The remainders have no secure optical classification. Given the smaller fraction of optical spectroscopic identifications in the EGS field, we also take into account the classification derived from spectral energy distribution (SED) fitting (Nandra et al. 2015) and include the sources dominated by unobscured QSO templates (i.e., where QSO emission is  $\geq 50\%$  of the total in the optical–near-IR bands) as BL AGNs (i.e., unobscured, type 1 AGNs) and sources dominated by galaxy or by obscured QSO templates as NL AGNs (i.e., obscured, type 2 AGNs). We find in total 18 BL AGNs and 21 NL AGNs (Table 1).

### 2.1. Spectral Extraction

The *NuSTAR* data have been processed using the standard *NuSTAR* Data Analysis Software (NuSTARDAS, v1.5.1) and calibration files (CALDB version 20131223), distributed within the NASA’s HEASARC software (HEASOFT v.6.17<sup>26</sup>). The source spectra have been extracted from each individual pointing using the task `nuproduct`, from circular extraction regions of  $45''$  radius (enclosing  $\sim 60\%$  of the *NuSTAR* point-spread function (PSF)); however, in crowded regions the extraction radius was reduced (to a minimum of  $30''$ ,  $\sim 45\%$  of the PSF) to minimize the contamination from nearby sources. The background spectra were extracted from four large regions ( $\approx 150''$  radius) lying in each of the four quadrants (CCDs) in each pointing, removing areas at the position of known bright *Chandra* sources ( $f_{2-8 \text{ keV}} > 5 \times 10^{-15} \text{ erg cm}^{-2} \text{ s}^{-1}$ ). The source and background spectra, as well as the ancillary files, were then combined using the task `addascaspec`.

The *Chandra* source spectra were extracted in a consistent way for all the fields, using the 250 ks and 4 Ms *Chandra* data in the E-CDFS (Lehmer et al. 2005; Xue et al. 2016) and CDFS (Xue et al. 2011), the 800 ks data in the EGS (Nandra et al. 2015) field, and the 1.8 Ms *Chandra* COSMOS (C-COSMOS; Elvis et al. 2009) and COSMOS-Legacy survey data (Civano et al. 2016). We used the *ACIS Extract* (AE) software

<sup>26</sup> <http://heasarc.nasa.gov/lheasoft/>

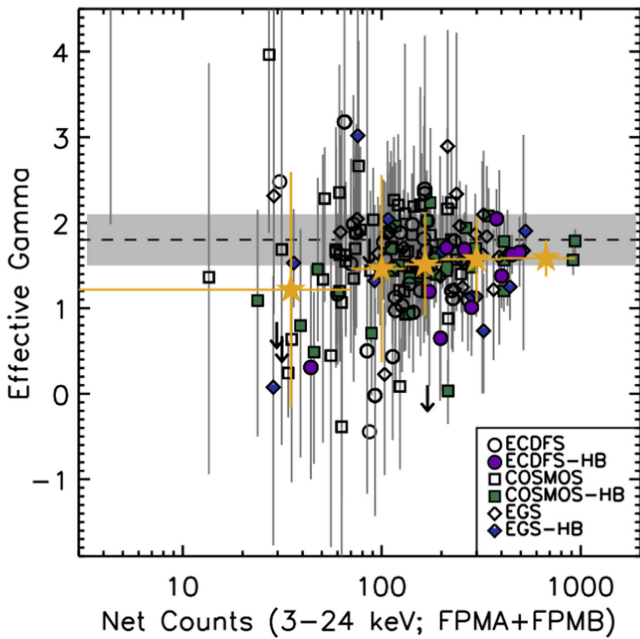


**Figure 2.** Effective photon index ( $\Gamma_{\text{eff}}$ ) vs. the net *NuSTAR* counts (FPMA+FPMB) for all the *NuSTAR*-detected sources in the E-CDFS (circles), EGS (diamonds), and COSMOS (squares) fields. The filled symbols indicate the sources that are significantly detected at  $E = 8\text{--}24$  keV (HB). The shaded region marks the intrinsic photon index  $\Gamma = 1.8 \pm 0.3$  typically found for AGNs (Nandra & Pounds 1994; Mainieri et al. 2002; Caccianiga et al. 2004; Mateos et al. 2005; Tozzi et al. 2006; Burlon et al. 2011). The effective photon index for our sources is derived by fitting a simple power-law model to the *NuSTAR* spectra of each individual source. For many sources the counting statistic is poor and the uncertainties on the  $\Gamma_{\text{eff}}$  are large. The stars represent the mean  $\Gamma_{\text{eff}}$  and standard deviation, in different net count bins.

package<sup>27</sup> (Broos et al. 2010; Broos et al. 2012) to extract the source spectra from individual observations using regions enclosing 90% of the PSF; background spectra and relative response matrices and ancillary files were also extracted and then combined by means of the *FTOOLS* `addrmf` and `addarf`.

### 3. Data Analyses

#### 3.1. Spectral Analysis

We first analyzed all the *NuSTAR* spectra ( $E \approx 3\text{--}25$  keV, observed frame) for each individual source to obtain a rough indication of the spectral slope. This is an essential step to produce the composite spectra (see Section 3.2). We therefore fitted all the spectra with a simple power-law model to obtain the effective photon index ( $\Gamma_{\text{eff}}$ ; Figure 2). Since we do not use any redshift information for this initial analysis, we performed the fit for all the *NuSTAR* sources in our sample. The FPMA and FPMB spectra were fitted simultaneously, with a renormalization factor free to vary, to account for the cross-calibration between the two detectors (Madsen et al. 2015). Due to the poor counting statistics characterizing most of our data (see Figure 2), the spectra have been lightly binned with a minimum of one count per energy bin, and the Cash statistic (C-stat; Cash 1979) was used. The median of the resulting effective photon index is  $\Gamma_{\text{eff}} = 1.57^{+0.79}_{-1.26}$  (the errors correspond

to the 5th and 95th percentiles). In Figure 2, we also show the mean  $\Gamma_{\text{eff}}$  (and  $1\sigma$  uncertainties) in various net count bins.

We then performed spectral fitting including the lower-energy spectra from *Chandra*. In this case we only include the sources matched to a *Chandra* counterpart and with redshift identification (173 sources). The *Chandra* data were fitted between 0.5 and 7 keV, and an absorbed power-law model including Galactic and intrinsic absorption was used. The Galactic column density was fixed to the mean values of  $N_{\text{H}}^{\text{Gal}} = 9.0 \times 10^{19} \text{ cm}^{-2}$ ,  $N_{\text{H}}^{\text{Gal}} = 1.05 \times 10^{20} \text{ cm}^{-2}$ , and  $N_{\text{H}}^{\text{Gal}} = 1.79 \times 10^{20} \text{ cm}^{-2}$  for E-CDFS, EGS, and COSMOS, respectively (Dickey & Lockman 1990), while the intrinsic absorption, the photon index ( $\Gamma$ ), and the relative normalization between *Chandra*, FPMA, and FPMB spectra were left free to vary. From these spectra we calculated the flux at 3–7 keV (observed frame), which is the overlapping energy range between the three telescopes, to test whether there is agreement between the *Chandra* and *NuSTAR* data sets (since they are not simultaneous), or whether variability might be an issue. In general, we found good agreement between the *Chandra* and *NuSTAR* fluxes within a factor of two (the mean *NuSTAR/Chandra* flux ratio and  $1\sigma$  error is  $1.1 \pm 0.5$ ); however, at the faint end the *NuSTAR* fluxes are systematically higher than the *Chandra* ones. This effect has already been shown by Mullaney et al. (2015) and Civano et al. (2015) and is consistent with the Eddington bias, which affects the fluxes close to the *NuSTAR* sensitivity limit.<sup>28</sup> Moreover, this effect could be partly due to the *NuSTAR* flux being a blend of multiple sources (see Section 2), while only one *Chandra* spectrum was analyzed together with the *NuSTAR* data. For the sources with multiple *Chandra* sources within the matching region, we performed the spectral fit of the *NuSTAR* data with each of the possible *Chandra* counterparts and then chose as a unique counterpart the *Chandra* source with the closest 3–7 keV flux, which is likely to give the highest contribution to the “blended” *NuSTAR* flux.

Since in several cases the spectral fit could not provide constraints on both  $N_{\text{H}}$  and  $\Gamma$  simultaneously, we fit the *Chandra* and *NuSTAR* data fixing  $\Gamma = 1.8$ , to obtain some constraints on the intrinsic column density. In some cases, when significant residuals are present at soft energies, we added another power-law component to the model, with the spectral slope fixed to that of the primary component (to limit the number of free parameters in the fits; e.g., Brightman et al. 2013; Lanzuisi et al. 2015; Del Moro et al. 2016), but not affected by intrinsic absorption, to account for any soft excess. From these spectra we also calculated the intrinsic X-ray luminosity at 10–40 keV ( $L_{10\text{--}40 \text{ keV}}$ , rest frame) as we aim to construct composite spectra in different bins of  $N_{\text{H}}$  and  $L_{10\text{--}40 \text{ keV}}$  (Sections 4.3 and 4.4). In Figure 3 we show the  $N_{\text{H}}$  versus  $L_{10\text{--}40 \text{ keV}}$  distribution for all the analyzed sources. For the composite spectra we will divide the sources into three column density bins (unabsorbed,  $N_{\text{H}} < 10^{22} \text{ cm}^{-2}$ , hereafter “NH1”; moderately absorbed,  $N_{\text{H}} = 10^{22}\text{--}10^{23} \text{ cm}^{-2}$ , hereafter “NH2”; and heavily absorbed,  $N_{\text{H}} > 10^{23} \text{ cm}^{-2}$ , hereafter “NH3”; see Section 4.3) and into three luminosity bins ( $L_{10\text{--}40 \text{ keV}} < 10^{44} \text{ erg s}^{-1}$ , hereafter “L1”;  $L_{10\text{--}40 \text{ keV}} = 10^{44}\text{--}10^{45} \text{ erg s}^{-1}$ , hereafter “L2”; and  $L_{10\text{--}40 \text{ keV}} \geq 10^{45} \text{ erg s}^{-1}$ , hereafter “L3”; see Section 4.4).

<sup>28</sup> For instance, the mean *NuSTAR/Chandra* flux ratio is  $2.2 \pm 2.6$  (median  $\approx 1.4$ ) for  $f_{3\text{--}7 \text{ keV}} < 5 \times 10^{-14} \text{ erg cm}^{-2} \text{ s}^{-1}$ , and it increases at the faintest fluxes, due to the effect of the Eddington bias (see Figure 11 from Civano et al. 2015; Figure 5 from Mullaney et al. 2015).

<sup>27</sup> The *ACIS Extract* software package and Users Guide are available at [http://www.astro.psu.edu/xray/acis/acis\\_analysis.html](http://www.astro.psu.edu/xray/acis/acis_analysis.html).

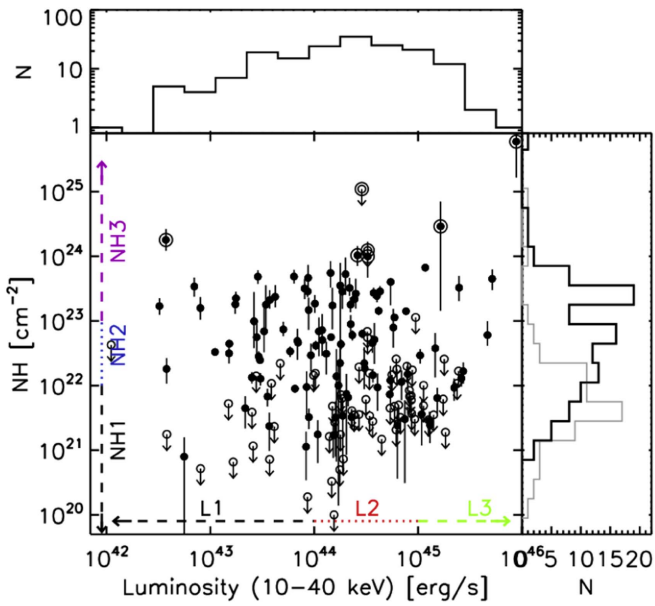


**Figure 3.** Hydrogen column density ( $N_{\text{H}}$ ) vs. the 10–40 keV luminosity derived for each individual source using an absorbed power-law model fitted to the *Chandra* plus *NuSTAR* spectra, with  $\Gamma = 1.8$  fixed. The open symbols indicate the  $N_{\text{H}}$  upper limits. On the left side of the panel the division in three different  $N_{\text{H}}$  bins is marked: NH1 ( $N_{\text{H}} < 10^{22} \text{ cm}^{-2}$ ), NH2 ( $N_{\text{H}} = 10^{22}\text{--}10^{23} \text{ cm}^{-2}$ ), and NH3 ( $N_{\text{H}} > 10^{23} \text{ cm}^{-2}$ ; see Section 4.3); at the bottom of the panel the division into three luminosity bins is indicated: L1 ( $L_{10\text{--}40 \text{ keV}} < 10^{44} \text{ erg s}^{-1}$ ), L2 ( $L_{10\text{--}40 \text{ keV}} = 10^{44}\text{--}10^{45} \text{ erg s}^{-1}$ ), and L3 ( $L_{10\text{--}40 \text{ keV}} \geq 10^{45} \text{ erg s}^{-1}$ ; see Section 4.4). Sources that are CT AGN candidates ( $N_{\text{H}} \gtrsim 10^{24} \text{ cm}^{-2}$ , within the uncertainties; see Section 5) are marked with larger open circles. The top panel shows the distribution of 10–40 keV luminosity of our sample sources. The right panel shows the  $N_{\text{H}}$  distribution, where the black histogram represents the measured  $N_{\text{H}}$ , while the gray histogram represents the  $N_{\text{H}}$  upper limits.

### 3.2. Composite Spectra

Given the faintness of the sources and the limited counting statistics, in many cases the spectral analysis of the individual sources does not provide constraints on the spectral parameters ( $\sim 40\%$  have  $N_{\text{H}}$  upper limits; see Figure 3). We therefore produce composite spectra in order to investigate the average properties of the AGNs detected by *NuSTAR*. We use both the *Chandra* and *NuSTAR* data together to produce the broadband composite spectra ( $\approx 2\text{--}40 \text{ keV}$ , rest frame), as the *Chandra* data help improve the counting statistics at low energies  $E \lesssim 7\text{--}10 \text{ keV}$  and allow us to obtain better constraints on the spectral properties than using the *NuSTAR* data alone.

#### 3.2.1. Averaging Method

The composite spectra were produced adopting the averaging method described in Corral et al. (2008). Briefly, using the best-fitting parameters obtained from the spectral fits described in the previous Section 3.1, i.e., an absorbed power law (with both  $N_{\text{H}}$  and  $\Gamma$  free) for the *Chandra*+*NuSTAR* spectra, we applied these models to the unbinned, background-subtracted spectra and saved the unfolded spectra in XSPEC (v.12.9.0) in physical units ( $\text{keV cm}^{-2} \text{ s}^{-1} \text{ keV}^{-1}$ ) in the energy range 3–25 keV for the *NuSTAR* data and between  $E = \max(0.5, 1.0/(1+z))$  and 7 keV for the *Chandra* data. We limit the *Chandra* spectra to energies above 1 keV (rest frame) to minimize the contribution from any soft component, which can create distortions in our composite spectra. Each spectrum was then shifted to the rest frame. To combine the

*Chandra* and *NuSTAR* data, we renormalize the *Chandra* spectra to the *NuSTAR* flux at 3–7 keV first, in order to correct for any flux differences, and apply a correction for the Galactic absorption. We then created a common energy grid for all the spectra, with at least 1200 summed counts per energy bin,<sup>29</sup> renormalized all the spectra to the flux in the rest-frame 8–15 keV energy range, and redistributed the fluxes in each new energy bin using Equations (1) and (2) from Corral et al. (2008). The renormalization of the spectra is necessary to avoid the brightest sources dominating the resulting composite spectra. We note that the resulting rescaled spectra preserve their spectral slopes and features. Instead of using the arithmetic mean to calculate the average flux in each new energy bin, as done by Corral et al. (2008), we took the median flux in each bin, as the median is less sensitive to outliers of the flux distribution (e.g., Falocco et al. 2012). In the Appendix we analyze in detail the differences between various averaging methods. To estimate the real scatter of the continuum, we performed a resampling analysis and produced 1000 composite spectra drawing random subsamples from the data (e.g., Politis & Romano 1994), excluding some of the spectra (at least one) each time (see Figure 4). For the final composite spectra we took the mean and standard deviation ( $1\sigma$ ) of the distribution of median fluxes obtained from the 1000 composite spectral realizations. In Figure 4 we also show the range of composite spectra (1st and 99th percentiles of the distribution) derived from the resampling analysis (shaded areas).

We note that the unfolding and the averaging process can distort the shape of the spectrum (e.g., Corral et al. 2008; Falocco et al. 2012). We therefore performed extensive simulations, which are described in the Appendix, to explore the effects of these distortions on the intrinsic average continuum and therefore to derive reliable results from our analyses.

## 4. Results

In this section we analyze our composite spectra for all of the sources, as well as for sources in different subsamples. All of the composite spectra have been fit using  $\chi^2$  statistics in the energy range  $E = 3\text{--}30 \text{ keV}$  (unless otherwise specified), as  $>60\%$  of the individual source spectra contribute at this energy range and the spectral simulations (see the Appendix) have shown that some distortions might affect the extremes of the composite spectra ( $E \approx 2\text{--}3 \text{ keV}$  and  $E > 30 \text{ keV}$ ), due to a smaller number of sources contributing to those energy bins. Moreover, the presence of some soft component can contribute to the composites at  $E \lesssim 3 \text{ keV}$  and therefore cause further distortions in the spectra. For our analysis we adopted three different models: (i) an absorbed power law with the addition of a Gaussian emission line at  $E \approx 6.4 \text{ keV}$  (defined hereafter as “baseline model”; `wabsxpow+Gauss`, in XSPEC formalism); (ii) a physically motivated torus model, such as TORUS (Brightman & Nandra 2011), which self-consistently includes the main iron emission lines and Compton scattering (hereafter “TORUS model”); and (iii) an absorbed power-law model with the addition of a Gaussian emission line and a reflection component (`wabsxpow+Gauss+pextrav`, in XSPEC formalism; Magdziarz & Zdziarski 1995), in order to constrain the reflection parameter ( $R$ ; hereafter “`pextrav` model”).

<sup>29</sup> The binning was chosen so that each source contributes, on average,  $\gtrsim 6\text{--}7$  counts per energy bin.

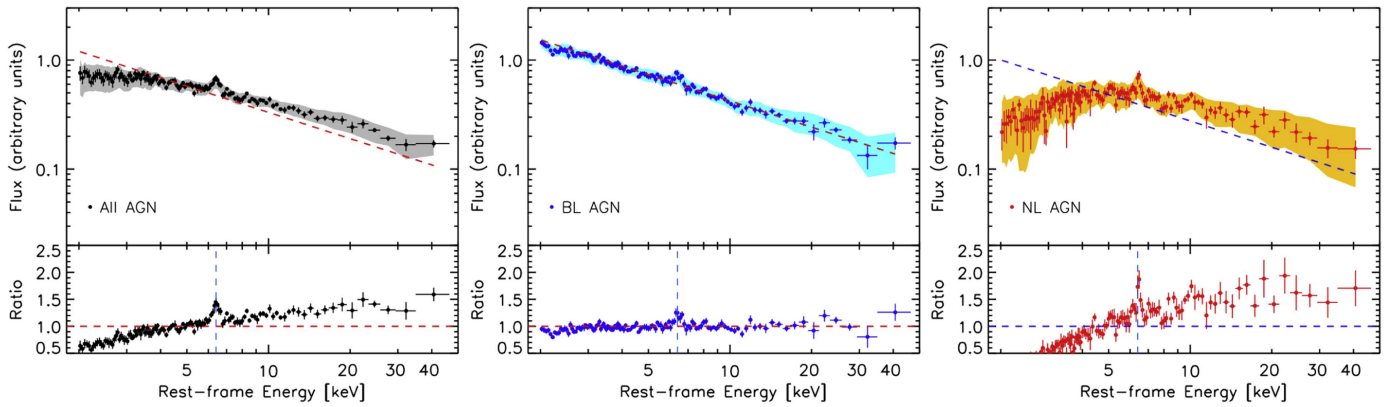


**Figure 4.** Composite spectra in the rest frame 2–40 keV obtained from the *Chandra* and *NuSTAR* data for all the *NuSTAR*-detected sources in the E-CDFS, EGS, and COSMOS fields (black circles; left); the middle and right panels show the composite spectra for sources classified in the optical band as BL AGNs (blue) and NL AGNs (red), respectively. The shaded areas in the three panels represent the range of the composite spectra (1st and 99th percentiles) obtained using a resampling analysis and calculating the median spectra 1000 times by randomly selecting subsamples of the sources. The dashed lines in the three panels represent a power-law model with a fixed index  $\Gamma = 1.8$ ; the power law is not fitted to the data, but is shown as a reference, by normalizing the flux to that of the composite spectra at  $E \approx 4\text{--}5$  keV. The bottom panels show the ratio between the spectra and the power law (dashed line). The vertical dashed lines mark the centroid of the iron  $K\alpha$  line at  $E \approx 6.4$  keV.

#### 4.1. Composite Spectra for BL and NL AGNs

Figure 4 shows the composite spectra from 2 keV to  $\sim 40$  keV (rest frame) of the *NuSTAR*+*Chandra* data. We produced a composite spectrum for all of the 173 sources with redshift identification (spectroscopic or photometric), and also for BL and NL AGNs separately. Since the number of sources involved in the BL and NL AGN composite spectra is low compared to the whole sample (see Table 1), the scatter in the spectra is larger. The *Chandra* data significantly improve the counting statistics at  $E \lesssim 10$  keV over the *NuSTAR*-only spectra and allow us to extend the composites to lower rest-frame energies in order to place constraints on the absorbing column densities, as well as on the intrinsic spectral slope. We initially fit these spectra with our baseline model, with both  $N_{\text{H}}$  and  $\Gamma$  free to vary. The model also includes a Gaussian emission line, as all three composite spectra clearly show an iron  $K\alpha$  emission line at  $E \approx 6.4$  keV. We fixed the line width to  $\sigma = 0.1$  keV (which is consistent with the values found for an unresolved Gaussian line in stacked spectra; see, e.g., Iwasawa et al. 2012; Falocco et al. 2013), while the central energy of the line was left free to vary, to account for possible scatter due to the use of photometric redshifts for some of our sources.<sup>30</sup> We caution that the hydrogen column densities derived from these spectra do not represent true median values, due to the nonlinear nature of the photoelectric absorption. The results of our spectral fits are reported in Table 2. We find a slightly flatter photon index for the composite of all the sources and for the NL AGNs ( $\Gamma = 1.65^{+0.03}_{-0.03}$  and  $\Gamma = 1.61^{+0.07}_{-0.07}$ , respectively) compared to the typical  $\Gamma \approx 1.8\text{--}2.0$ . On the other hand, the BL AGN spectral slope is in good agreement with the typical values ( $\Gamma = 1.78^{+0.03}_{-0.02}$ ).

<sup>30</sup> We tested the fits also using a narrow Gaussian line fixed at  $E = 6.4$  keV and width free to vary in the range  $\sigma = 0.01\text{--}0.2$  keV (e.g., Corral et al. 2008). However, the line width typically pegs at the high limit, as several factors can contribute to broaden the line, such as (i) the stacking process (e.g., Corral et al. 2008; Falocco et al. 2013), (ii) the possible inaccuracy of photometric redshifts, and (iii) the presence of a broad component. All these effects could be investigated and disentangled using simulations; however, this is beyond the scope of this paper. For simplicity, we therefore fix the line width to  $\sigma = 0.1$  keV and leave the energy free, to account for some of the uncertainties on the line.

From extensive spectral simulations (see the Appendix), performed to assess the distortions and variations of the true spectral shape, which might occur at different stages of the stacking process, and thus to validate our spectral analysis results, we find that by simulating unabsorbed *NuSTAR* and *Chandra* spectra with a fixed  $\Gamma = 1.8$ , the resulting composite spectrum has a photon index of  $\Gamma = 1.77\text{--}1.83$ , in good agreement with the slope of the input simulated spectra. This is true also combining unabsorbed spectra with a range of power-law slopes ( $\Gamma = 1.6\text{--}2.0$ ; see the Appendix). On the other hand, combining spectra with different levels of X-ray absorption (and therefore different photoelectric cutoff energies) does affect the intrinsic slope of the composite spectra, which becomes slightly flatter ( $\Gamma \approx 1.72\text{--}1.76$ ; Appendix) than the input  $\Gamma = 1.8$  of the simulated spectra. This is because the absorption features, which occur at different energies depending on the  $N_{\text{H}}$  values, are “smoothed” during the stacking process, producing an artificial flattening of the spectral slope (as the true intrinsic  $N_{\text{H}}$  cannot be recovered). We note, however, that in every test we performed with our simulations we find that this effect is not large enough to explain the relatively flat  $\Gamma$  values observed in the composite spectra from the real data. We can therefore assess that the flattening of spectral slope of the NL AGN composite is real and is significantly different from the slope seen for the BL AGNs. An absorbed power-law model with  $\Gamma \approx 1.61$ , in fact, provides a better fit to the data than a slope of  $\Gamma = 1.8$  at the  $>99.9\%$  confidence level, according to the  $F$ -test probability. We then fit the data with the TORUS model (Brightman & Nandra 2011), where we fixed the torus opening angle<sup>31</sup> to  $\theta_{\text{tor}} = 30^\circ$  for all of the spectra, while we fixed the inclination angle to  $\theta_{\text{inc}} = 60^\circ$  for the BL AGNs and  $\theta_{\text{inc}} = 80^\circ$  (nearly edge-on) for the NL AGNs, as these parameters cannot be constrained in the fit. We note that changing the  $\theta_{\text{inc}}$  value for the BL AGNs to, e.g.,  $30^\circ$  makes little difference to the model and to the resulting spectral parameters (the differences are within the parameter uncertainties). We obtain consistent results with those of the baseline

<sup>31</sup> We chose an opening angle of  $\theta_{\text{tor}} = 30^\circ$  because it provides the highest emission-line equivalent width (EW) allowed by this model (Brightman & Nandra 2011). Despite this, we find that an extra emission-line component is still needed to reproduce the data.

**Table 2**  
Spectral Parameters of the Composite Spectra in Different  $N_{\text{H}}$  and Luminosity Bins

Bin	No.	WA×PO+GAUSS				TORUS			WA×PO+GAUSS+PEXRAV			
		$\Gamma$	$N_{\text{H}}^{\text{a}}$	EW (eV)	$\chi^2/\text{dof}$	$\Gamma$	$N_{\text{H}}^{\text{a}}$	$\chi^2/\text{dof}$	$\Gamma$	$N_{\text{H}}^{\text{a}}$	$R$ ( $R_{\Gamma=1.8}$ )	$\chi^2/\text{dof}$
All	173	$1.65^{+0.03}_{-0.03}$	$1.8^{+0.5}_{-0.5}$	$92^{+22}_{-22}$	86.1/90	$1.66^{+0.04}_{-0.05}$	$1.4^{+0.5}_{-0.4}$	88.5/90	$1.65^{+0.05}_{-0.05}$	$1.8^{+0.5}_{-0.5}$	$<0.17$ ( $0.47^{+0.15}_{-0.11}$ )	86.1/89
BL	76	$1.78^{+0.03}_{-0.02}$	$<0.3$	$75^{+21}_{-21}$	94.3/90	$1.79^{+0.01}_{-0.01}$	$<2.7$	93.7/90	$1.84^{+0.08}_{-0.06}$	$<0.7$	$<0.64$ ( $0.12^{+0.10}_{-0.11}$ )	91.8/89
NL	69	$1.61^{+0.05}_{-0.05}$	$5.8^{+1.0}_{-1.0}$	$105^{+41}_{-41}$	89.5/90	$1.60^{+0.08}_{-0.05}$	$4.8^{+0.8}_{-0.8}$	93.0/90	$1.62^{+0.05}_{-0.07}$	$5.8^{+1.0}_{-1.0}$	$<0.15$ ( $0.46^{+0.32}_{-0.30}$ )	89.5/89
HB	64	$1.62^{+0.05}_{-0.05}$	$1.6^{+0.7}_{-0.7}$	$76^{+25}_{-25}$	110.0/90	$1.61^{+0.06}_{-0.03}$	$1.2^{+0.6}_{-0.6}$	113.1/90	$1.62^{+0.10}_{-0.03}$	$1.6^{+0.8}_{-0.7}$	$<0.39$ ( $0.67^{+0.22}_{-0.21}$ )	110.0/89
SB	79	$1.69^{+0.05}_{-0.05}$	$1.7^{+0.7}_{-0.7}$	$97^{+30}_{-30}$	75.2/90	$1.74^{+0.13}_{-0.15}$	$1.8^{+1.4}_{-1.4}$	33.7/90	$1.69^{+0.07}_{-0.03}$	$1.7^{+0.7}_{-0.7}$	$<0.25$ ( $0.30^{+0.22}_{-0.21}$ )	75.2/89
NH1	86 <sup>b</sup>	$1.78^{+0.02}_{-0.02}$	$<0.3$	$62^{+21}_{-21}$	84.0/90	$1.79^{+0.02}_{-0.01}$	$<0.2$	84.1/90	$1.80^{+0.08}_{-0.03}$	$<0.5$	$<0.43$ ( $<0.23$ )	83.5/89
NH2	44 <sup>b</sup>	$1.68^{+0.08}_{-0.08}$	$2.4^{+0.9}_{-0.9}$	$101^{+39}_{-43}$	59.2/90	$1.69^{+0.07}_{-0.10}$	$2.1^{+0.8}_{-0.8}$	58.7/90	$1.72^{+0.18}_{-0.09}$	$2.5^{+1.2}_{-1.1}$	$<1.08$ ( $0.52^{+0.39}_{-0.36}$ )	59.0/89
NH3	39 <sup>b</sup>	$1.64^{+0.12}_{-0.11}$	$28.4^{+3.6}_{-3.3}$	$100^{+60}_{-66}$	114.1/77	$1.38^{+0.12}_{-0.12}$	$16.2^{+2.2}_{-2.6}$	184.7/79	$1.64^{+0.14}_{-0.11}$	$28.3^{+3.7}_{-3.3}$	$<0.34$ ( $<0.71$ )	114.1/76
L1	61 <sup>b</sup>	$1.49^{+0.10}_{-0.10}$	$1.8^{+1.3}_{-1.3}$	$115^{+53}_{-53}$	81.9/90	$1.52^{+0.07}_{-0.12}$	$1.7^{+1.1}_{-1.1}$	81.5/90	$1.51^{+0.17}_{-0.06}$	$1.8^{+1.5}_{-1.3}$	$<0.67$ ( $1.19^{+0.57}_{-0.50}$ )	81.9/89
L2	84 <sup>b</sup>	$1.71^{+0.04}_{-0.04}$	$1.5^{+0.6}_{-0.6}$	$100^{+29}_{-17}$	98.8/90	$1.72^{+0.04}_{-0.05}$	$1.2^{+0.6}_{-0.5}$	102.6/90	$1.71^{+0.10}_{-0.03}$	$1.5^{+0.8}_{-0.6}$	$<0.34$ ( $0.29^{+0.17}_{-0.16}$ )	98.8/89
L3	22 <sup>b</sup>	$1.73^{+0.05}_{-0.03}$	$<0.6$	$70^{+38}_{-37}$	77.4/90	$1.75^{+0.04}_{-0.03}$	$<0.6$	72.0/90	$1.86^{+0.19}_{-0.13}$	$<1.5$	$<1.74$ ( $0.34^{+0.22}_{-0.22}$ )	70.2/89

**Notes.**

<sup>a</sup> The column density  $N_{\text{H}}$  is expressed in units of  $10^{22} \text{ cm}^{-2}$ .

<sup>b</sup> Median value of the number of sources in each bin, resulting from 1000 spectral realizations with randomized  $N_{\text{H}}$  or  $L_X$  values within their error range.

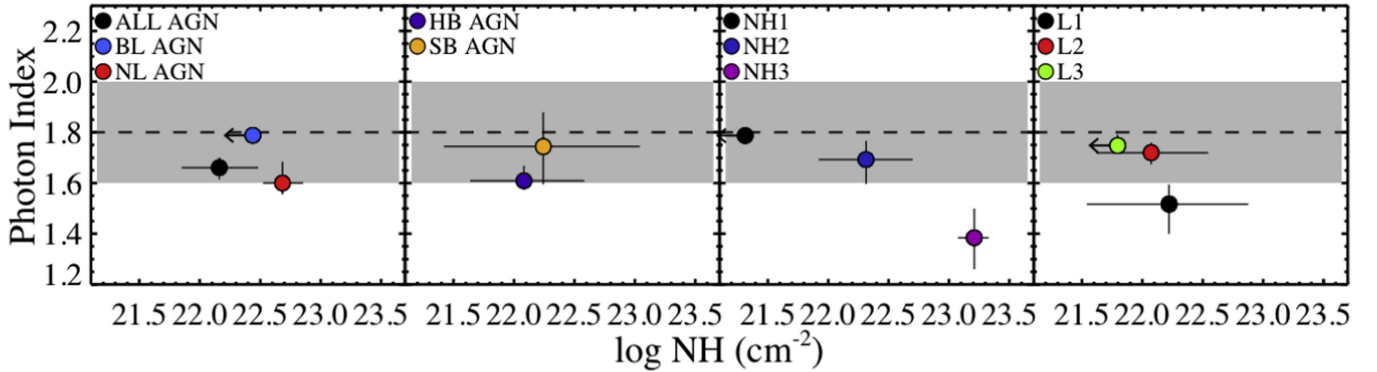


**Figure 5.** Photon index vs. hydrogen column density ( $N_{\text{H}}$ ) derived by fitting the TORUS model to each of our composite spectra. From left to right the panels show the results for (i) all the sources (black), BL AGNs (blue), and NL AGNs (red), as described in Section 4.1; (ii) HB-detected (purple) and SB-detected (orange) AGNs (see Section 4.2); (iii) different  $N_{\text{H}}$  bins (NH1: black; NH2: blue; NH3: magenta), described in Section 4.3; and (iv) different 10–40 keV luminosity bins (L1: black; L2: red; L3: green), as described in Section 4.4. The gray shaded area represents the typical AGN photon index of  $\Gamma = 1.8 \pm 0.2$ .

model, with a flattened photon index for the composite spectra of all the sources and of the NL AGNs ( $\Gamma = 1.66^{+0.04}_{-0.05}$  and  $\Gamma = 1.60^{+0.08}_{-0.05}$ , respectively), compared to that of the BL AGNs ( $\Gamma = 1.79^{+0.01}_{-0.01}$ ; see Figure 5). We note, however, that significant residuals in the spectra suggest that the addition of a Gaussian emission line is necessary for all three composite spectra, as the best-fitting TORUS model does not fully account for the iron line emission seen in our spectra. This suggests that possibly also a Compton reflection component is not fully represented by this model, which could explain the resulting slightly flat indices.

Indeed, there are two main effects that can produce a flattening in the spectral slope: (1) photoelectric absorption at soft X-ray energies, which can be underestimated and therefore compensated in the fit by a flatter  $\Gamma$  (e.g., Mateos et al. 2005); and (2) Compton reflection contributing to the flux at  $E > 10$  keV (e.g., Bianchi et al. 2009; Ballantyne et al. 2011). The reflection component may arise from either the accretion disk or cold, dense gas at large distances from the nucleus, such as from the inner part of the putative obscuring torus (e.g., Ross & Fabian 2005; Murphy et al. 2009). To verify how much the reflection can be contributing to our composite

spectra, we then used the pexrav model, as described above. In this model we fixed the photon index of the pexrav component to be the same as that of the primary power law  $\Gamma = \Gamma_{\text{ref}} = 1.8$  (assuming that the NL AGNs have intrinsically the same spectral slope as the BL AGNs), the inclination angle to a mean value of  $\cos \theta = 0.45$ , and the power-law cutoff energy to  $E_c = 200$  keV (e.g., Ballantyne 2014). We constrain the reflection parameter<sup>32</sup> to be  $R = 0.46^{+0.32}_{-0.30}$  for the NL AGNs, while for the BL AGNs we obtained  $R = 0.12^{+0.10}_{-0.11}$  (see Figure 6). From the composite of all the sources we obtained  $R = 0.47^{+0.15}_{-0.14}$  ( $\Gamma = 1.8$  fixed). Although the scatter on the constraints for the NL AGNs is relatively large, this shows that a larger contribution from a reflection component in the NL AGNs compared to the BL AGNs could indeed be responsible for the flattening of the spectral slope.

From the composite spectra we also derived the EW of the iron  $K\alpha$  emission line at  $E \approx 6.4$  keV. As stated above, the

<sup>32</sup> In our model we force  $R$  to be negative, so the pexrav component represents a pure reflection component, decoupled from the primary power-law model. However, in the text we report the absolute value of the reflection parameter.

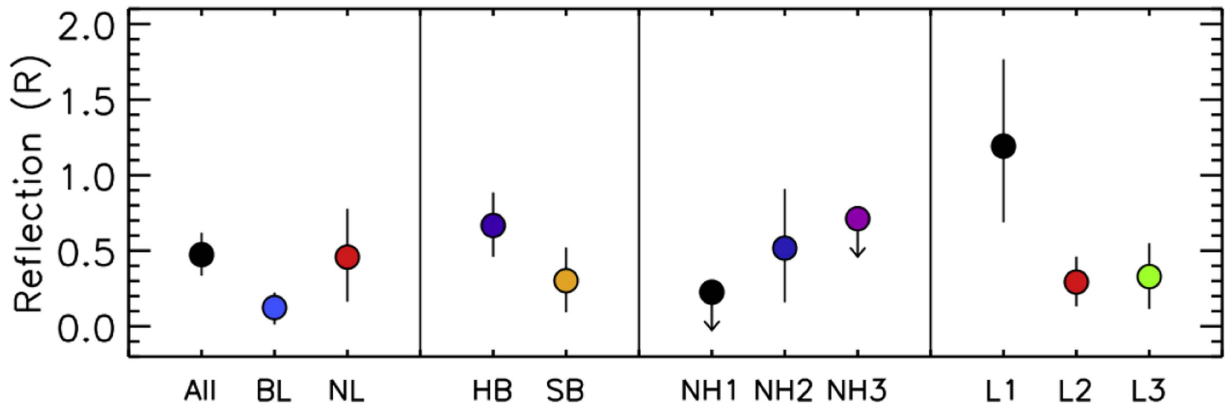


**Figure 6.** Reflection fraction ( $R$ ) derived from the spectral fit of the composite spectra using the baseline model with the addition of a reflection component ( $wabs \times po + pexrav + Gauss$ ) and photon index fixed at  $\Gamma = 1.8$ . Symbols are the same as in Figure 5.

central energy was left free to vary in the fits to allow for the uncertainties that might arise from using photometric redshifts, while the line width was fixed to  $\sigma = 0.1$  keV. The resulting centroid of the emission line is always at  $E \approx 6.4$  keV with typical scatter of  $\Delta E \lesssim 0.05$  keV. The obtained EWs (reported in Table 2) from our composite spectra are broadly in agreement with the results from previous works that have investigated the composite X-ray spectra of AGNs (e.g., Corral et al. 2008; Falocco et al. 2012; Liu et al. 2016). For the NL AGNs we find slightly higher EW values than for the BL AGNs, which is consistent with the trend seen for the strength of the reflection component; however, given the uncertainties, the trend for the iron line EW is only tentative. Moreover, although some broadening and complexities of the line are visible in the spectra, we only fit a single narrow emission line, since it has been shown that the averaging process and the rest-frame shifting of all the spectra can cause broadening and distortions of the emission line and of the underlying continuum (e.g., Yaqoob 2007; Corral et al. 2008; Falocco et al. 2012). Spectral simulations of the emission line would be required to assess the true nature of these complexities. However, since the detailed properties of the emission line are not the main focus of our paper, we do not attempt more complex analyses.

#### 4.2. Comparison between *NuSTAR* Hard-band- and Soft-band-detected AGNs

With our analyses we also aim to test whether there are significant differences between the intrinsic spectral properties of the sources detected in the *NuSTAR* HB (8–24 keV) and those that formally are not (i.e., they are undetected according to the threshold used by Mullaney et al. 2015; Civano et al. 2015). We then produced a composite spectrum for all the 64 HB-detected sources (see Table 1) and for the soft-band (SB; 3–8 keV) detected sources that are HB undetected (79 sources) and fit the spectra with the models described in the previous section. The spectra are shown in Figure 7. Using our baseline model, the resulting spectral parameters for the HB composite spectrum are  $\Gamma = 1.62^{+0.05}_{-0.05}$  and  $N_H = (1.6 \pm 0.7) \times 10^{22} \text{ cm}^{-2}$ , with a fairly weak emission line (EW =  $76 \pm 25$  eV). For the SB composite spectrum the best-fitting parameters are  $\Gamma = 1.69^{+0.05}_{-0.05}$  and  $N_H = (1.7 \pm 0.7) \times 10^{22} \text{ cm}^{-2}$ , with an EW of the iron  $K\alpha$  emission line of EW =  $97 \pm 30$  eV. Adopting the TORUS model yields

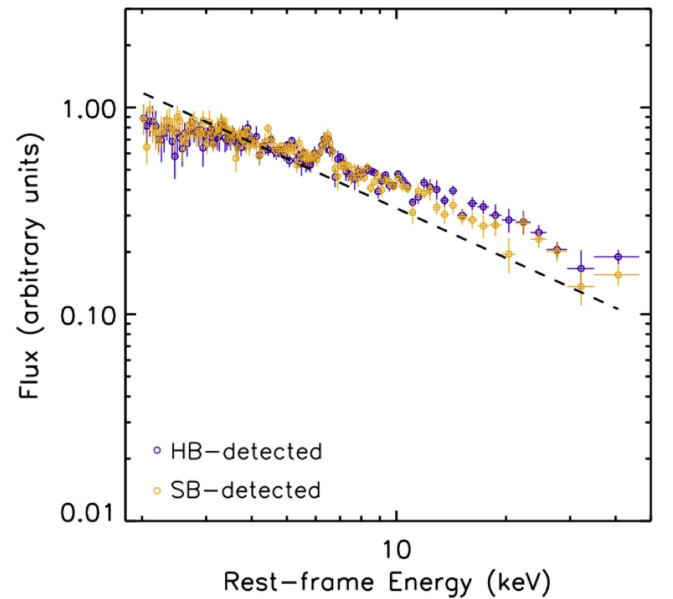


**Figure 7.** Composite spectra in the rest-frame 2–40 keV energy range for sources detected in the *NuSTAR* HB (purple) and those that are not HB detected (SB; orange). The dashed line in the panel represents a power law with  $\Gamma = 1.8$ .

consistent results for the spectral slope and intrinsic  $N_H$  with our baseline model (see Figure 5 and Table 2).

Using the *pexrav* model, as described in the previous section, we constrain  $\Gamma = 1.62^{+0.10}_{-0.03}$  and  $R < 0.39$  ( $R = 0.67^{+0.22}_{-0.21}$  for  $\Gamma = 1.8$  fixed) for the HB-detected sources; the spectral parameters are consistent within the uncertainties with those obtained for the SB-detected sources, i.e.,  $\Gamma = 1.69^{+0.07}_{-0.03}$  and  $R < 0.25$  ( $R = 0.30^{+0.22}_{-0.21}$  for  $\Gamma = 1.8$  fixed; Figure 6). If we attempt to account for the “artificial” flattening due to the stacking process, e.g., by fixing  $\Gamma = 1.76$  (instead of  $\Gamma = 1.8$ ; see the Appendix), the constraints on the reflection parameters become  $R = 0.50^{+0.20}_{-0.19}$  for the HB composite spectrum and  $R < 0.37$  for the SB composite spectrum. Although there is a hint of an increase of the reflection strength in the composite spectrum of the HB-detected sources, the spectral parameters of the HB- and SB-detected sources are consistent within the uncertainties. These results therefore suggest that the two subsamples have similar characteristics, with no significant

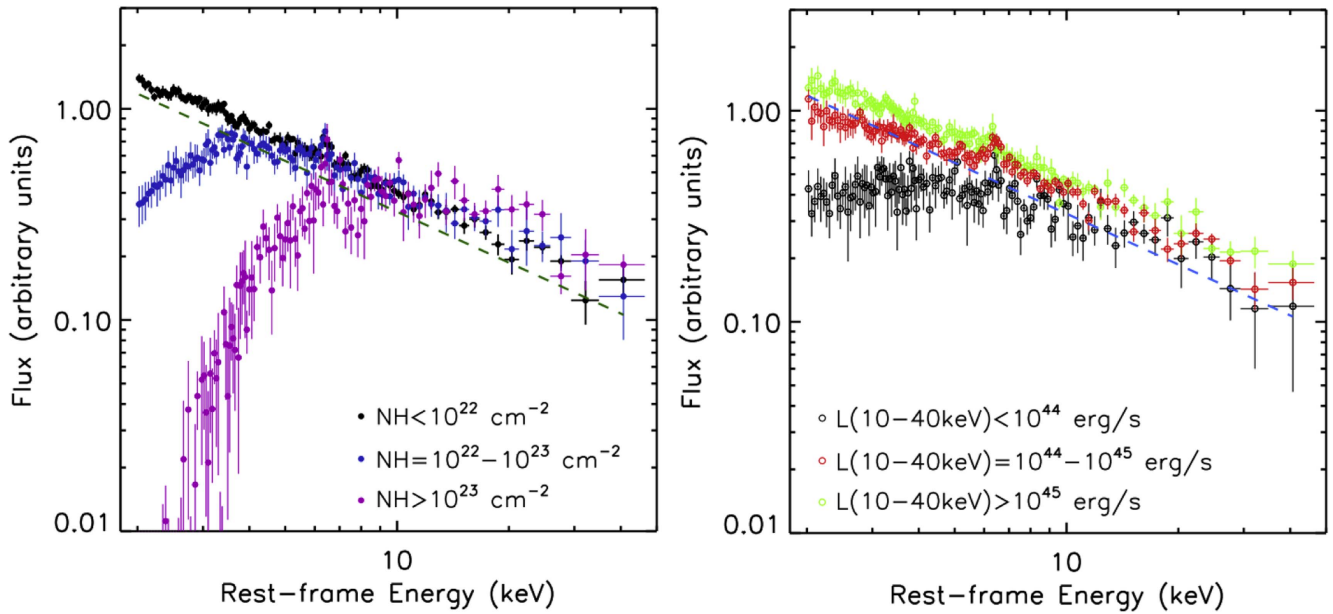


**Figure 8.** Left: composite spectra in the rest-frame 2–40 keV energy range for sources in different  $N_{\text{H}}$  bins:  $N_{\text{H}} < 10^{22} \text{ cm}^{-2}$  (unabsorbed; black),  $N_{\text{H}} = 10^{22}\text{--}10^{23} \text{ cm}^{-2}$  (moderately absorbed; blue), and  $N_{\text{H}} > 10^{23} \text{ cm}^{-2}$  (heavily absorbed; magenta). Right: composite spectra in the rest-frame 2–40 keV energy range for sources with  $L_{10\text{--}40 \text{ keV}} < 10^{44} \text{ erg s}^{-1}$  (black),  $L_{10\text{--}40 \text{ keV}} = 10^{44}\text{--}10^{45} \text{ erg s}^{-1}$  (red), and  $L_{10\text{--}40 \text{ keV}} \geq 10^{45} \text{ erg s}^{-1}$  (green). The dashed line in both panels represents a power law with  $\Gamma = 1.8$ .

biases toward more obscured or reflection-dominated objects in the HB-detected samples compared to the SB-detected samples (the fraction of X-ray-obscured sources in the two subsamples is  $\sim 52\%$  and  $\sim 46\%$ , respectively).

#### 4.3. Average Spectral Properties for Absorbed and Unabsorbed AGNs

To place better constraints on the contribution from Compton reflection to the average spectra of the *NuSTAR* sources and disentangle its effect from that of absorption in flattening the spectral slope (see Section 4.1), we produce composite spectra in different  $N_{\text{H}}$  bins. In this way, by knowing a priori the median  $N_{\text{H}}$  of the spectra, we can attribute any hardening of the spectral slope just to the strength of the Compton hump. As an estimate of the intrinsic  $N_{\text{H}}$  of the sources we used the results from the fitting of the *Chandra* and *NuSTAR* spectra for individual sources with  $\Gamma = 1.8$  fixed (see Figure 3 and Section 3.1). We caution that this is a very simple model and provides a crude estimate of the column densities, as more complex models might be needed to fully characterize the individual source spectra (e.g., Del Moro et al. 2014; L. Zappacosta et al. 2017, in preparation). However, such analysis is not feasible for many of the sources given the limited counting statistics.

We divided the sources into three  $N_{\text{H}}$  bins (see Section 3.1):  $N_{\text{H}} < 10^{22} \text{ cm}^{-2}$  (NH1),  $N_{\text{H}} = 10^{22}\text{--}10^{23} \text{ cm}^{-2}$  (NH2), and  $N_{\text{H}} > 10^{23} \text{ cm}^{-2}$  (NH3), including upper limits. To distribute the sources in each bin, we approximated the  $N_{\text{H}}$  and errors of each source to a Gaussian distribution and performed 1000 spectral realizations, randomly picking an  $N_{\text{H}}$  value from the distribution and assigning the source to one of the three  $N_{\text{H}}$  bins accordingly. For the sources with an  $N_{\text{H}}$  upper limit ( $\sim 40\%$  of the sample; see Figure 3) we assumed a constant probability distribution for the column density values ranging from  $\log N_{\text{H}} = 20.5 \text{ cm}^{-2}$  and the  $N_{\text{H}}$  upper limit of the source. We

excluded two (absorbed) sources owing to their particularly strong soft component and/or spectral complexity, which would further increase the scatter of the composite spectra at  $E \lesssim 4 \text{ keV}$  and around the iron line. The median number of sources in each bin, resulting from the 1000 spectral realizations, is 86 in NH1, 44 in NH2, and 39 in NH3 (see Table 2). As described in Section 3.2.1, the final average spectra are obtained taking the mean and the  $1\sigma$  standard deviation of the distribution of median fluxes in each energy bin, resulting from the 1000 spectral realizations described above, and resampling analysis. We note that the NH3 bin has typically a smaller number of sources compared to the other two, and therefore the scatter in the composite spectrum is larger. The composite spectra in the three different bins are shown in Figure 8 (left panel).

We again fit the data with our baseline model and with the TORUS model, including a Gaussian line. The spectrum in the NH3 bin was fitted between 3.5 and 30 keV, as the spectrum at  $E < 3.5 \text{ keV}$  has large scatter (see Figure 8, left panel), likely due to the presence of a soft-scattered component in some of the individual source spectra. The two models yield fairly consistent results, which are summarized in Table 2. From the fit we obtained values of  $N_{\text{H}}$  consistent with the median values in each bin for all three composite spectra, while we find a significant flattening of the spectral slope for the NH3 sources (with the highest  $N_{\text{H}}$ ), especially with the TORUS model, compared to the unabsorbed and moderately absorbed sources (NH1 and NH2), for which the spectral slopes are consistent with the typical values of  $\Gamma = 1.8 \pm 0.2$  (see Figure 5). We note, however, that the fitting statistic for the NH3 composite spectrum is poor (see Table 2), and therefore the constraints on the spectral parameters for the sources in this  $N_{\text{H}}$  bin are less reliable than for the sources with lower X-ray absorption.

To constrain the contribution from the Compton reflection component to the composite spectra, we used the `pexrav`

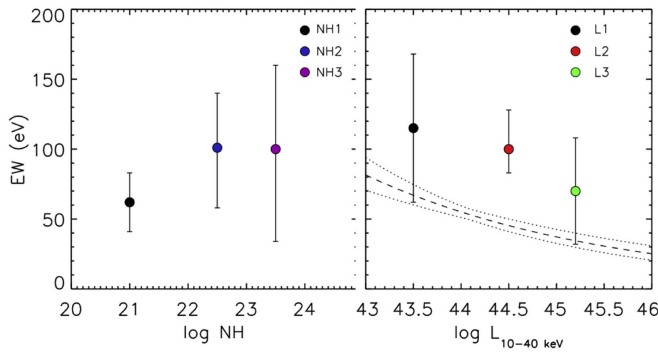


**Figure 9.** EW of the iron  $K\alpha$  line measured from our composite spectra. The width of the line was fixed to  $\sigma = 0.1$  keV in all cases. The left panel shows the EW as a function of  $N_H$ , derived from the composite spectra in the NH1, NH2, and NH3 bins. The right panel shows the EW as a function of the 10–40 keV luminosity measured from the composite spectra in the L1, L2, and L3 bins. The dashed and dotted lines show the anticorrelation between the strength of the iron  $K\alpha$  line and the X-ray luminosity (“Iwasawa-Taniguchi effect”; Iwasawa & Taniguchi 1993), as measured by Bianchi et al. (2007), and the combined errors on the slope and normalization of their best fit. Their 2–10 keV luminosity has been converted here to the 10–40 keV luminosity using a power-law model with  $\Gamma = 1.8$ .

model, as in the previous sections (see Sections 4.1 and 4.2). For the NH1 spectrum the best-fit parameters are  $\Gamma = 1.80^{+0.08}_{-0.03}$  and  $N_H < 0.5 \times 10^{22} \text{ cm}^{-2}$ , with a relative reflection fraction upper limit of  $R < 0.43$  ( $\chi^2/\text{dof} = 83.5/89$ ; see Table 2). For the NH2 spectrum the best-fit parameters are  $\Gamma = 1.72^{+0.18}_{-0.09}$  and  $N_H = (2.5^{+1.2}_{-1.1}) \times 10^{22} \text{ cm}^{-2}$ , with a relative reflection fraction upper limit of  $R < 1.08$  ( $\chi^2/\text{dof} = 59.0/89$ ). For the NH3 spectrum the best-fitting solution still favors a slightly flatter photon index of  $\Gamma = 1.64^{+0.14}_{-0.11}$  (although still consistent with typical values within the errors) and  $N_H = (28.3^{+3.7}_{-3.3}) \times 10^{22} \text{ cm}^{-2}$ , with a low reflection fraction upper limit of  $R < 0.34$  ( $\chi^2/\text{dof} = 114.1/76$ ).

Since the spectral parameters  $\Gamma$  and  $R$  are somewhat degenerate when the scatter in the spectra is large (e.g., Del Moro et al. 2014), we then fixed the photon index to  $\Gamma = 1.8$ , i.e., the intrinsic value found for the unobscured and BL AGNs, to obtain better constraints on the reflection fraction. From these spectral fits we obtained  $R < 0.23$  for the NH1 spectrum,  $R = 0.52^{+0.39}_{-0.36}$  for the NH2 spectrum, and  $R < 0.71$  for the NH3 spectrum (see Figure 6;  $R < 0.51$  if we fix  $\Gamma = 1.75$  to account for the “artificial” flattening of the composite spectra with high  $N_H$ ). The contribution from reflection is typically low in unobscured sources (NH1), while it seems to increase in obscured sources (e.g., Ricci et al. 2011; Vasudevan et al. 2013). The relatively poor fit obtained for the NH3 composite spectrum, however, does not allow us to place tight constraints on  $R$  and therefore to securely assess whether there is a clear dependence between the strength of the Compton reflection and  $N_H$ . This is true also for the EW of the iron  $K\alpha$  line (see Table 2 and Figure 9, left panel). Although we would expect an increase of EW with absorption (as the EW is measured against the absorbed continuum), we cannot find a significant dependence, due to the large errors on our EW measurements. We note, however, that the EW of the iron line in the three  $N_H$  bins has a similar trend to that of the reflection strength (see Figure 6), despite these two components being fitted independently in our models. This is expected, since the iron line and the Compton hump are two features of the same reflection spectrum.

#### 4.4. Luminosity Dependence of the X-Ray Spectral Properties

To test whether the average spectral parameters of the *NuSTAR* sources change as a function of luminosity, we constructed composite spectra in three different luminosity bins: L1, i.e., sources with  $L_{10-40 \text{ keV}} < 10^{44} \text{ erg s}^{-1}$ ; L2, with  $L_{10-40 \text{ keV}} = 10^{44} - 10^{45} \text{ erg s}^{-1}$ ; and L3, with  $L_{10-40 \text{ keV}} \geq 10^{45} \text{ erg s}^{-1}$ . Similarly to the method adopted in the previous section, we have approximated the luminosity  $L_{10-40 \text{ keV}}$  and its uncertainties for each source with a Gaussian probability function and performed 1000 realizations randomly picking a  $L_{10-40 \text{ keV}}$  value from the distribution and assigning the source to each luminosity bin. For the luminosity upper limits we assumed again a constant probability function ranging from  $\log L_{10-40 \text{ keV}} = 42.0$  to the corresponding upper-limit value of the source. From the 1000 realizations the median number of sources in each bin is 61 in L1, 84 in L2, and 22 in L3 (see Table 2). In this case, although the L3 bin has a small number of sources, the composite spectrum has a fairly high signal-to-noise ratio (S/N), as the sources in this bin are brighter and have typically good counting statistics in each individual spectrum. On the other hand, the L1 composite spectrum has relatively high scatter since it comprises the least luminous sources in the sample and therefore the S/N of the individual spectra is typically lower than those in the other luminosity bins. Figure 8 (right panel) shows the composite spectra in the three luminosity bins.

Fitting the spectra with our baseline model, we find that for low-luminosity sources the photon index is flatter ( $\Gamma_{L1} = 1.49^{+0.10}_{-0.10}$ ) than those of higher-luminosity sources ( $\Gamma_{L2} = 1.71^{+0.04}_{-0.04}$  and  $\Gamma_{L3} = 1.73^{+0.05}_{-0.03}$ ). All the best-fitting spectral parameters are reported in Table 2. Similar results are obtained when using the TORUS model to fit the spectra (Figure 5). The flattening of the spectrum of the L1 sources might be due to a higher incidence of absorbed sources in this luminosity bin ( $\sim 57\%$ , compared to  $\sim 47\%$  and  $\sim 36\%$  in the L2 and L3 bins, respectively). Indeed, the median value of the column density at  $L_{10-40 \text{ keV}} < 10^{44} \text{ erg s}^{-1}$  is  $N_H(L1) \approx 2.5 \times 10^{22} \text{ cm}^{-2}$ , while for the other two luminosity bins the values are lower:  $N_H(L2) \approx 8.1 \times 10^{21} \text{ cm}^{-2}$  and  $N_H(L3) \approx 6.4 \times 10^{21} \text{ cm}^{-2}$ . However, a K-S test on the  $N_H$  distribution in the three luminosity bins (see Figure 3) suggests that the distributions are not significantly different ( $D(L1-L2) = 0.178$  and  $\text{Prob}(L1-L2) = 0.227$ , and  $D(L1-L3) = 0.240$  and  $\text{Prob}(L1-L3) = 0.278$ ).

Some studies have found a dependence of the photon index on luminosity, where high-luminosity sources show steeper  $\Gamma$  than the low-luminosity ones (e.g., Dai et al. 2004; Saez et al. 2008). Conversely, other studies have found an anticorrelation between  $\Gamma$  and X-ray luminosity (e.g., Corral et al. 2011; Scott et al. 2011). Some of these trends are probably a consequence of the stronger dependence that has been found for the photon index with Eddington ratio (e.g., Brightman et al. 2013; Ricci et al. 2013b). The flat photon index we found for the L1 spectrum might be partly due to these correlations. However, the spectral slopes of the sources in the L2 and L3 luminosity bins are pretty much the same (see Figure 5 and Table 2), and therefore there is no clear dependence of  $\Gamma$  on luminosity in our sample (e.g., Winter et al. 2009; Brightman et al. 2013).

We therefore investigate whether there is any difference in the amount of Compton reflection contributing to the spectra as a function of luminosity. We fit the `pexrav` model to our spectra, as in the previous sections (Sections 4.1 and 4.3), and we constrain the spectral parameters to be  $\Gamma = 1.51^{+0.17}_{-0.06}$ ,

**Table 3**  
Spectral Parameters of the Composite *Chandra*+*NuSTAR* Spectra for the Low- and High-luminosity Sources, Further Divided into Unobscured (unob) and Obscured (obs), Fitted with Our `pexrav` Model, `wabsxpow+Gauss+pexrav`

Bin	No. <sup>a</sup>	$\log L_{10-40 \text{ keV}}^b$	$z^c$	$\Gamma$	$N_{\text{H}}^d$	EW (eV)	$R$ ( $R_{\Gamma=1.8}$ )	$\chi^2/\text{dof}$
Low-L unob	39	43.95	0.698	$1.80^{+0.10}_{-0.07}$	$<1.4$	$103^{+45}_{-38}$	$<0.36$ ( $<0.24$ )	71.2/89
Low-L obs	48	43.84	0.660	$1.42^{+0.12}_{-0.10}$	$6.5^{+1.2}_{-1.9}$	$118^{+70}_{-69}$	$<0.30$ ( $1.35^{+0.73}_{-0.60}$ )	91.8/89
High-L unob	46	44.81	1.342	$1.85^{+0.06}_{-0.05}$	$<0.5$	$68^{+23}_{-25}$	$0.39^{+0.40}_{-0.31}$ ( $0.12^{+0.12}_{-0.11}$ )	83.4/89
High-L obs	33	44.63	1.375	$1.73^{+0.22}_{-0.17}$	$8.4^{+2.3}_{-2.2}$	$106^{+62}_{-50}$	$<1.65$ ( $0.71^{+0.43}_{-0.38}$ )	42.5/89

#### Notes.

<sup>a</sup> Number of spectra used for the composite; this is the median value obtained from the 1000 spectral realizations.

<sup>b</sup> Logarithm of the median X-ray luminosity (10–40 keV) of the sources in each bin.

<sup>c</sup> Median redshift of the sources in each bin.

<sup>d</sup> The hydrogen column density is expressed in units of  $10^{22} \text{ cm}^{-2}$ .

$N_{\text{H}} = (1.8^{+1.5}_{-1.3}) \times 10^{22} \text{ cm}^{-2}$ , and  $R < 0.67$  for the L1 sources;  $\Gamma = 1.71^{+0.10}_{-0.03}$ ,  $N_{\text{H}} = (1.5^{+0.8}_{-0.6}) \times 10^{22} \text{ cm}^{-2}$ , and  $R < 0.34$  for the L2 sources; and  $\Gamma = 1.86^{+0.19}_{-0.13}$ ,  $N_{\text{H}} < 1.5 \times 10^{22} \text{ cm}^{-2}$ , and  $R < 1.74$  for the L3 sources, which is basically unconstrained. Fixing the photon index  $\Gamma = 1.8$ , we obtain tighter constraints on the reflection fraction in the three luminosity bins, i.e.,  $R = 1.19^{+0.57}_{-0.50}$ ,  $R = 0.29^{+0.17}_{-0.16}$ , and  $R = 0.34^{+0.22}_{-0.22}$  for the L1, L2, and L3 sources, respectively (see Figure 6). While for the low-luminosity sources ( $L_{10-40 \text{ keV}} < 10^{44} \text{ erg s}^{-1}$ ) the reflection strength is relatively high, we find that it decreases significantly at luminosities  $L_{10-40 \text{ keV}} \geq 10^{44} \text{ erg s}^{-1}$  (e.g., Bianchi et al. 2007; Shu et al. 2010; Liu et al. 2016; however, see also Vasudevan et al. 2013). Although this trend is only seen fixing the photon index, due to the degeneracies in the spectral parameters, this decrease is significant also if we fit the L1 spectrum with a flatter photon index of  $\Gamma = 1.75$  to correct for the “artificial” flattening discussed in the previous sections, which yields  $R = 0.93^{+0.52}_{-0.47}$ . We find hints of a similar, decreasing trend also for the EW of the iron  $K\alpha$  line measured from the composite L1, L2, and L3 spectra (see Figure 9, right panel), although, given the large errors, this trend is not statistically significant. An anticorrelation between the strength of the Fe  $K\alpha$  line and the X-ray luminosity has been observed and investigated in several previous studies (e.g., Iwasawa & Taniguchi 1993; Nandra et al. 1997; Page et al. 2004; Bianchi et al. 2007; Ricci et al. 2013a), and it is often referred to as the “X-ray Baldwin effect” or the “Iwasawa-Taniguchi effect” (IT effect). We compared our results with the anticorrelation found by Bianchi et al. (2007) for a sample of radio-quiet, type 1 AGNs (dashed and dotted lines in Figure 9, right panel). We converted their 2–10 keV luminosity into the 10–40 keV luminosity assuming a power-law model with  $\Gamma = 1.8$ . The slope of the anticorrelation is consistent with our results; however, the EWs we find in our spectra are typically larger compared to those found by Bianchi et al. (2007). This is likely due to the different types of analyses and different types of sources (as we also include absorbed AGNs) used in the two papers, as the measurements from our stacking analyses might be biased toward higher values of EW compared to the distribution found from individual sources. Moreover, the emission line in our composite spectra is broadened owing to the rest-frame shifting of the spectra (see Section 3.2.1), thus likely increasing the measured EW.

If the IT effect is due to a decrease of the covering factor with increasing AGN luminosity (e.g., Bianchi et al. 2007), this

could also explain the drop of the reflection strength, as in high-luminosity sources there is less material close to the nucleus obscuring/reflecting the intrinsic X-ray emission, thus producing a weaker Compton reflection spectrum. We caution, however, that we cannot exclude that the drop of  $R$  at high luminosities could be partly due to an evolution of the spectral properties with redshift, as the mean redshifts of the sources in the L1, L2, and L3 luminosity bins are  $\langle z \rangle = 0.55$ ,  $\langle z \rangle = 1.17$ , and  $\langle z \rangle = 1.86$ , respectively.

#### 4.5. Compton Reflection Strength and Iron $K\alpha$ Line

Even dividing the sources into bins of column density or X-ray luminosity, it is not possible to fully understand how the average spectral properties, such as the strength of the iron  $K\alpha$  line and the Compton reflection, depend on these two quantities, as  $N_{\text{H}}$  and  $L_{\text{X}}$  are somewhat linked. For instance, the NH1 bin contains a larger fraction of high-luminosity sources ( $\sim 74\%$ ) compared to the NH2 and NH3 bins ( $\sim 67\%$  and  $\sim 59\%$ , respectively). Similarly, the L1 bin has a larger fraction of absorbed sources than the high-luminosity bins (see Section 4.4). To further investigate how the Compton reflection might depend on luminosity and/or  $N_{\text{H}}$  independently, we divided the sources into two luminosity bins,  $L_{10-40 \text{ keV}} < 2 \times 10^{44} \text{ erg s}^{-1}$  and  $L_{10-40 \text{ keV}} \geq 2 \times 10^{44} \text{ erg s}^{-1}$ ; the separation was chosen to have a comparable number of sources within the low- and high-luminosity bins (see Table 3). Within these bins we produce separate composite spectra for the unabsorbed ( $N_{\text{H}} < 10^{22} \text{ cm}^{-2}$ ) and absorbed ( $N_{\text{H}} \geq 10^{22} \text{ cm}^{-2}$ ) sources. We adopted the same randomization method described in Sections 4.3 and 4.4 to assign sources to each bin. Since our aim here is to investigate the reflection component, we only fit the composite spectra with the `pexrav` model. The resulting parameters are reported in Table 3. In Figure 10 (left panel) we show the reflection parameter ( $R$ ) derived from this analysis as a function of the rest-frame 10–40 keV luminosity; for each composite spectrum, we plot the median  $L_{10-40 \text{ keV}}$  of the sources. The uncertainties on the derived spectral parameters are quite large, especially for the obscured sources, and therefore it is not possible to derive a statistically significant dependence of  $R$  on luminosity or  $N_{\text{H}}$ ; however, there is an indication of a decreasing trend with luminosity. Moreover, the unobscured sources seem to have typically a smaller reflection fraction than the obscured ones. These trends seem to be confirmed by the strength of the iron line measured from these spectra, as shown in Figure 10 (right panel), where the iron line EW is plotted against  $R$ . The

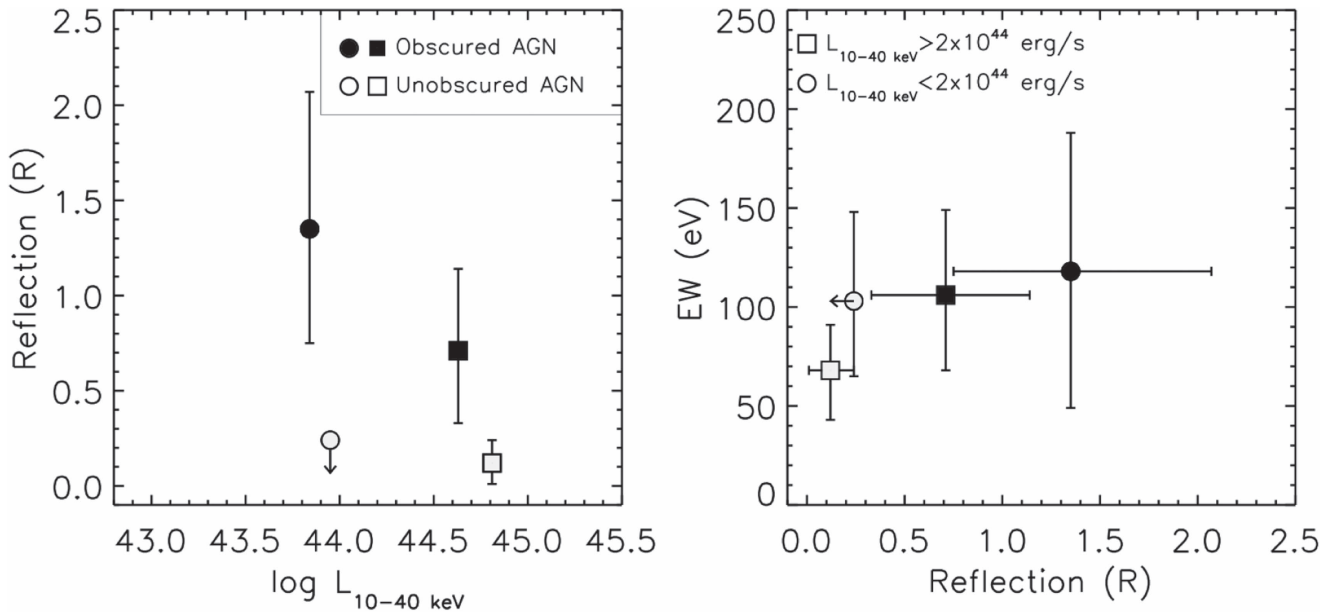


**Figure 10.** Left: reflection fraction ( $R$ ) as a function of the rest-frame 10–40 keV luminosity derived from the composite spectra of the low-luminosity sources ( $L_{10-40 \text{ keV}} < 2 \times 10^{44} \text{ erg s}^{-1}$ ; circles) and high-luminosity sources ( $L_{10-40 \text{ keV}} > 2 \times 10^{44} \text{ erg s}^{-1}$ ; squares), divided into unobscured (i.e.,  $N_{\text{H}} < 10^{22} \text{ cm}^{-2}$ ; open symbols) and obscured ( $N_{\text{H}} \geq 10^{22} \text{ cm}^{-2}$ ; filled symbols) sources. Although the error bars are large, there seems to be a decreasing trend of  $R$  both with increasing luminosity and with decreasing  $N_{\text{H}}$ . Right: iron  $\text{K}\alpha$  line EW vs. the reflection fraction ( $R$ ), for the same luminosity and  $N_{\text{H}}$  bins.

strength of the emission line for obscured and unobscured sources seems to follow a similar behavior to the Compton reflection strength. Indeed, a Spearman rank correlation test, performed on 10,000 simulated data sets accounting for the uncertainties of the data points, indicates that there is a strong correlation, as the resulting correlation coefficient is  $\rho_s = 0.80$ ; however, given the small number of data points and the large uncertainties, the null hypothesis probability is  $P = 0.38$ .

### 5. CT AGNs in the *NuSTAR* Survey

From the spectral analysis of the *Chandra* and *NuSTAR* data of the individual sources in our sample using a simple absorbed power-law model with  $\Gamma = 1.8$  fixed (Section 3.1), we identified seven sources with column densities consistent (within the errors) with CT values ( $N_{\text{H}} \gtrsim 10^{24} \text{ cm}^{-2}$ ; see Figure 3). One of these sources (*NuSTAR* ID 330 in Civano et al. 2015) was indeed identified as a CT AGN by Civano et al. (2015) from the spectral analysis of the *NuSTAR*, *Chandra*, and *XMM-Newton* data available for this source. For the other six sources (*NuSTAR* ID 8 in E-CDFS; IDs 129, 153, 189, and 216 in COSMOS; and ID 22 in EGS), which have typically lower-S/N spectra with both *NuSTAR* (<150 net counts, FPMA+FPMB) and *Chandra* (<100 net counts), we cannot place tight constraints on the spectral parameters (for two of these sources we only have an upper limit on  $N_{\text{H}}$ ), and thus we are not able to confirm their CT nature individually. The sources *NuSTAR* IDs 129, 153, 189, and 22, which are matched to the *Chandra* counterparts (CIDs) 284, 1021, and 875 in COSMOS (Elvis et al. 2009) and CID 718 in EGS (Nandra et al. 2015), respectively, have been already identified as heavily obscured sources by Brightman et al. (2014), with only CID 718 having a column density consistent with CT values within the uncertainties.

Performing the spectral analysis of the individual sources, with the addition of *XMM-Newton* data to the *NuSTAR* and *Chandra* data, L. Zappacosta et al. (2017, in preparation)

constrained IDs 129 and 216 in COSMOS to be heavily obscured, but not CT AGNs. We therefore exclude these sources from our list of CT AGN candidates.

For the remaining five sources, we therefore performed joint spectral fitting (see, e.g., Alexander et al. 2013), in an attempt to place better constraints on the average spectral parameters, as well as the reflection fraction, of these CT AGN candidates. In this case we do not produce a composite spectrum because, given the small number of sources, it would be dominated by the uncertainties. We note, however, that the joint spectral fitting method is analogous to the spectral fitting of the composite spectra for deriving the average spectral parameters. We initially fit the *Chandra* ( $E = 0.5\text{--}7 \text{ keV}$ ) and *NuSTAR* data ( $E = 3\text{--}25 \text{ keV}$ ) using an absorbed power-law model including Galactic and intrinsic absorption, with  $\Gamma$  and  $N_{\text{H}}$  free to vary, and a narrow Gaussian line with  $E = 6.4 \text{ keV}$  and  $\sigma = 0.05 \text{ keV}$ , analogous to the baseline model we used to fit the composite spectra. Since we include softer energies compared to those of the composite spectra, we also include a soft component, parameterized, for simplicity, as a power law with the same photon index as the primary, absorbed power law:  $\text{wabs} \times (\text{po} + \text{zwabs} \times \text{po} + \text{zgauss})$ . With this model, the resulting best-fitting parameters are  $\Gamma = 1.81^{+0.38}_{-0.35}$  and  $N_{\text{H}} = (1.5^{+0.8}_{-0.6}) \times 10^{24} \text{ cm}^{-2}$ , i.e., consistent with the CT regime, as derived originally from the spectral fit of the individual sources. Due to the low counting statistics of the spectra, the iron emission line could not be constrained, as its EW resulted in a limit of  $\text{EW} < 0.7 \text{ keV}$ . This is not necessarily in contrast with the presence of CT absorption, as some CT AGNs have been reported to have unusually weak Fe lines (e.g., Gandhi et al. 2017). To allow for the spectral complexity expected for these heavily obscured sources, we used the TORUS model, with an inclination angle fixed at  $\theta_{\text{inc}} = 80^\circ$  and a torus opening angle fixed at  $\theta_{\text{tor}} = 60^\circ$ , with the addition of a soft-scattered power law. The resulting photon index and hydrogen column density,  $\Gamma = 1.91^{+0.59}_{-0.41}$  and

$N_{\text{H}} = (9.6^{+8.6}_{-4.9}) \times 10^{23} \text{ cm}^{-2}$ , are in good agreement with the results from the previous model, within the uncertainties.

To constrain the amount of reflection in these CT AGN candidates, we resort again to the `pexrav` model with the addition of a soft-scattered component. The resulting power-law slope is  $\Gamma = 1.88^{+1.13}_{-0.22}$ , and the column density is  $N_{\text{H}} = (1.5^{+1.3}_{-0.6}) \times 10^{24} \text{ cm}^{-2}$ , consistent with the CT regime; the reflection fraction, however, is not well constrained in these spectra,  $R < 3.64$  ( $R < 2.22$  for fixed  $\Gamma = 1.8$ ).

Comparing these results with those obtained for the composite spectrum of the sources in the NH3 bin (which also includes typically the five sources analyzed here), there seems to be disagreement in the obtained parameters, especially the flattening trend of the photon index (see Figure 5 and Section 4.3), since from the joint fitting we obtain steeper  $\Gamma$  than those obtained from the NH3 composite (Figure 6). We note, however, that the spectral slopes are consistent within the uncertainties. Moreover, we need to account for the fact that the composite spectra in the NH3 bin are only fitted above 3.5 keV (rest frame), while for the joint fit we also include softer-energy data. To allow for a fair comparison between the results, we tested our joint-fitting analysis limiting the data to the same energy range used in the composite spectra (and removing the soft power-law component from the model). The baseline model in this case yields a much flatter photon index of  $\Gamma = 0.72^{+0.54}_{-0.46}$  and  $N_{\text{H}} < 2.3 \times 10^{23} \text{ cm}^{-2}$ . Similarly, performing a joint fit with the `pexrav` model, in the same energy range covered by the composite spectra (i.e., rest frame  $E \geq 3.5$  keV for the NH3 bin), we obtained  $\Gamma = 0.97^{+0.52}_{-0.36}$ ,  $N_{\text{H}} = < 2.1 \times 10^{23} \text{ cm}^{-2}$ , and a reflection fraction of  $R < 1.01$  ( $R > 0.98$  for  $\Gamma = 1.8$  fixed). Within the large uncertainties, these parameters could be broadly consistent with the values and obtained from the NH3 composite spectrum (Figure 6); however, for  $\Gamma = 1.8$  we only obtain a lower limit on  $R$  for the CT AGN candidates. The poor constraints obtained for the parameters in these two spectral fits suggest that the soft-scattered component is still needed for such high column densities and might also partly explain the flat photon index obtained for the NH3 bin spectrum. We argue that when the broader energy range is used in the joint-fitting analysis, the photon index is mainly constrained by the soft-energy component. This could bias the results, as the soft component can be produced by various processes, not necessarily related to the nuclear AGN emission (e.g., star formation in the host galaxy), and have steeper slope than the intrinsic power law. On the other hand, the small number of photons detected from the heavily absorbed primary AGN emission leads to the degeneracy between  $\Gamma$  and  $N_{\text{H}}$ , as described in Section 4.1.

## 6. Compton Reflection and the CXB

Several previous works have highlighted the problem of parameter degeneracies in the synthesis models of the CXB (e.g., Gandhi et al. 2007; Treister et al. 2009; Akylas et al. 2012) and of the model's assumptions for the XLF (e.g., Aird et al. 2015a), which prevent us from deriving important constraints, such as the fraction of CT AGNs contributing to the CXB and their space density. Among all the parameters, the amount of Compton reflection assumed in the spectral models yields the largest uncertainty on the CT AGN population (Akylas et al. 2012). Besides directly observing and identifying CT AGNs in the available X-ray surveys and measuring directly the true  $N_{\text{H}}$  distribution of AGNs at all redshifts, which

has proved to be challenging even with the deepest data, the only solution to break these degeneracies is to better measure the intrinsic spectral properties of the AGN population, and in particular the Compton reflection fraction. Such measurements have been performed in the local universe using *Swift*-BAT and *INTEGRAL* observatories (Molina et al. 2009; Burlon et al. 2011; Ricci et al. 2011; Vasudevan et al. 2013; Ballantyne 2014; Esposito & Walter 2016), which are sensitive to the hard X-ray energies needed to directly probe the peak of the Compton reflection hump ( $E \approx 20\text{--}30$  keV, rest frame). However, *NuSTAR* is the only observatory available to date that allows such studies at higher redshifts ( $z \approx 1$ ), thanks to its higher sensitivity ( $\sim 2$  orders of magnitude) at  $E > 10$  keV compared to previous observatories.

The measurements we obtained from our composite spectra for the full *NuSTAR* AGN sample ( $R \approx 0.5$ ; see Section 4.1 and Figure 6), for typical  $\Gamma = 1.8$ , are lower than the Compton reflection strength measured for sources in the local universe. For instance, Ballantyne (2014), who investigated the mean 0.5–200 keV spectrum of local AGNs, found an average reflection strength of  $R = 1.7^{+1.7}_{-0.9}$ , consistent with several previous works (e.g., Molina et al. 2009; Burlon et al. 2011; Ricci et al. 2011; Vasudevan et al. 2013). It is important to note, however, that the samples investigated in the local universe are usually dominated by Seyfert galaxies (i.e., with  $L_{\text{X}} < 10^{44} \text{ erg s}^{-1}$ ), while in our sample the vast majority of the sources ( $\sim 70\%$ ) are quasars ( $L_{\text{X}} > 10^{44} \text{ erg s}^{-1}$ ), for which we constrain a much weaker reflection fraction than for the lower-luminosity AGNs. On the other hand, the results we obtain for the  $L_{\text{X}} < 10^{44} \text{ erg s}^{-1}$  AGNs (L1 bin) are in good agreement with the above-mentioned studies in the local universe, possibly indicating that there is no significant evolution of the source spectra, and therefore of their intrinsic physical properties, between redshift  $z \approx 0$  and  $z \approx 1$  (the median redshift of our sample).

To compare our results with the typical assumptions made by several AGN synthesis models of the CXB (e.g., Ueda et al. 2003; Ballantyne et al. 2006; Gilli et al. 2007; Treister et al. 2009; Ueda et al. 2014), we performed here several spectral fits with photon index fixed at various typical values ( $\Gamma = 1.8 \pm 0.2$ , usually assumed in the CXB models) to obtain better constraints on the amount of Compton reflection in our composite spectra for each assumed spectral slope. This is to overcome the degeneracy we found between  $\Gamma$  and  $R$  (Section 4.3). In Figure 11 we show the constraints on  $R$  as a function of the assumed spectral slope for each of the three  $N_{\text{H}}$  bins (left panel; see Section 4.3) and for the three luminosity bins (right panel; see Section 4.4). In general, at all  $\Gamma$ , we do not find a significant difference in  $R$  between the three  $N_{\text{H}}$  bins (when high- and low-luminosity sources are combined together); for relatively flat photon indices  $\Gamma = 1.6\text{--}1.8$ , the reflection fraction tends to be below 1, while for steeper  $\Gamma$  it might reach values up to  $R \approx 1.5\text{--}2.0$  for the obscured sources (NH2 and NH3), considering the uncertainties, and  $R \approx 1$  for the unobscured ones (NH1).

The same analysis in the three luminosity bins (Figure 11, right panel) shows that at all photon indices  $R$  tends to be higher for the low-luminosity sources (L1) than for the high-luminosity ones (L2 and L3; see Section 4.4). For flat photon indices ( $\Gamma \leq 1.7$ ), at high luminosities (L2 and L3), the reflection fraction is consistent with  $R = 0$ , while for steeper photon indices ( $\Gamma = 1.8\text{--}2.0$ ) we find significant reflection

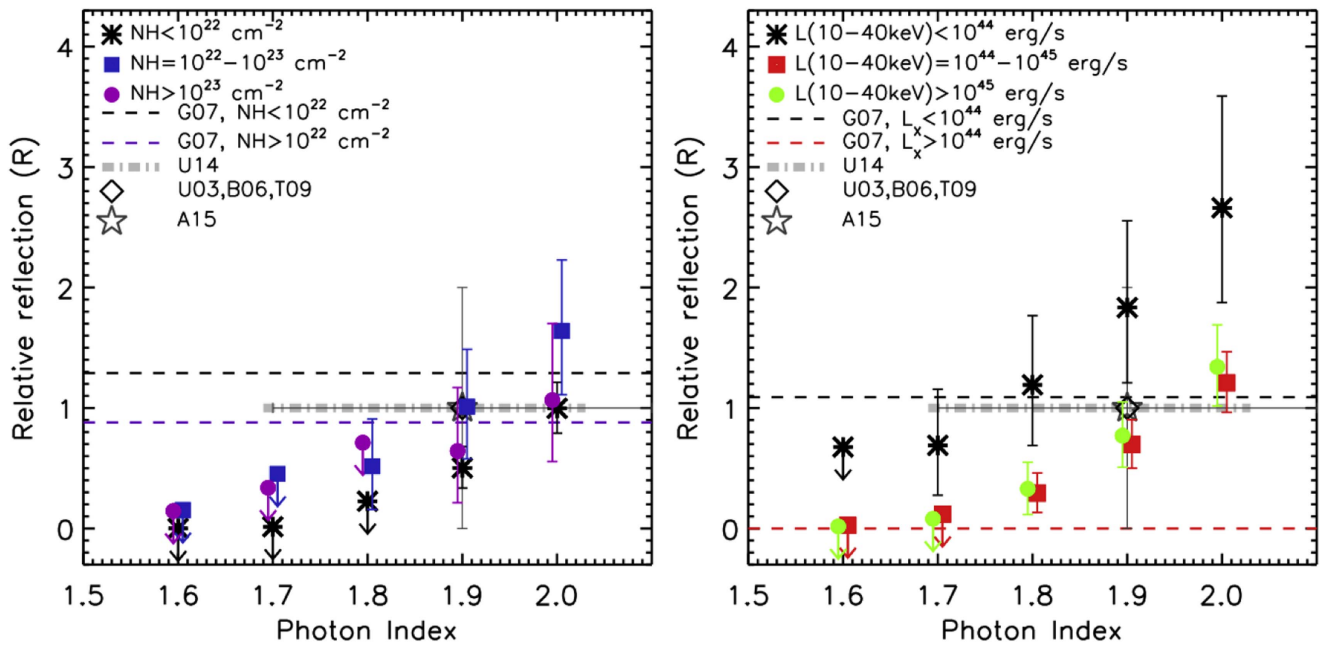


**Figure 11.** Left: relative reflection strength ( $R$ ) as a function of photon index ( $\Gamma$ ) assumed in the model for the composite spectra in the three  $N_{\text{H}}$  bins: NH1 (black asterisks), NH2 (blue squares), and NH3 (magenta circles). The errors and upper limits are estimated at a 90% confidence level. Right:  $R$  vs.  $\Gamma$  in the three luminosity bins: L1 (black asterisks), L2 (red squares), and L3 (green circles). In the panels we indicate the AGN spectral model parameters assumed in various CXB population synthesis models and XLF studies: Gilli et al. (2007) (G07; dashed lines); Ueda et al. (2014) (U14; dot-dashed line); Ueda et al. (2003), Ballantyne et al. (2006), and Treister et al. (2009) (U03, B06, and T09, respectively; black diamond); and Aird et al. (2015a) (A15; gray star).

fractions also for the high-luminosity sources  $R \approx 0.3$ – $1.3$ . At low luminosities (L1), the reflection fraction ranges from  $R \approx 0.7$  to  $R \approx 2.7$  (at steeper photon indices).

Most of the CXB models adopt a photon index of  $\Gamma = 1.9$  and  $R = 1$  in their parameterization of the intrinsic spectra for all AGNs, with no difference in luminosity and/or  $N_{\text{H}}$  (e.g., Ueda et al. 2003, 2014; Ballantyne et al. 2006; Treister et al. 2009). On the other hand, Gilli et al. (2007) assume different reflection fractions for absorbed and unabsorbed AGNs with  $L_{\text{X}} < 10^{44}$  erg s $^{-1}$  ( $R = 0.88$  and  $R = 1.3$ , respectively, following Comastri et al. 1995), implying that the reflection is mainly due to scattered radiation from the accretion disk; for all quasars ( $L_{\text{X}} > 10^{44}$  erg s $^{-1}$ ) they assume  $R = 0$ .

Our findings are in line with the assumptions made in the Gilli et al. (2007) model for the high- and low-luminosity sources; however, there are some differences, which could potentially have an impact in the models. For instance, Gilli et al. (2007) assume a larger reflection fraction for unobscured AGNs compared to the obscured AGNs, while from our analyses, at low luminosities, the obscured sources seem to have slightly larger  $R$  values (see Figure 10, left panel). Moreover, although the reflection fraction we find for the high-luminosity sources is small ( $R \approx 0.3$  for  $\Gamma = 1.8$ ; see Figure 11), it makes a contribution of  $\sim 12\%$  to the flux at 10–40 keV compared to a model with  $R = 0$ . Conversely, a reflection fraction of  $R = 1$ , as assumed by the above-mentioned models for all AGNs, is consistent with our values for the low-luminosity AGNs (although higher  $R$  values should also be allowed in the models, according to our results). However, it would overestimate the reflection contribution for the high-luminosity AGNs, compared to our results, by  $\approx 10\%$ – $20\%$  in the 10–40 keV flux. These differences might not have a big impact on the CXB models, as the majority of the contribution to the CXB spectrum comes from low-luminosity sources ( $\sim 75\%$  from  $L_{\text{X}} < 10^{44}$  erg s $^{-1}$  AGNs according to the model from Gilli et al. 2007). However,

detailed modeling, accounting for all these differences, and folding in the AGN XLF are necessary to reliably assess whether there are significant discrepancies between our results and the typical assumptions of the CXB synthesis models and how much our constraints on  $R$  would impact these models. For instance, higher (lower) values of  $R$  in the CXB models would require a smaller (larger) fraction of CT AGNs to reproduce the CXB spectrum peak at  $E \approx 20$ – $30$  keV, and this would place important constraints on the overall accreting black hole population in the universe.

Aird et al. (2015a) compared two different models of the XLF by Aird et al. (2015b) and Ueda et al. (2014) to reproduce the number of sources observed by *NuSTAR*. The main differences between the models are in the assumed  $N_{\text{H}}$  distribution and in the fraction of CT AGNs among the total AGN population. They find that both models can reproduce the observations; however, in the Ueda et al. (2014) model a large contribution from Compton reflection ( $R \approx 2$ ) in the source spectra would be necessary to obtain good agreement with the observations (Aird et al. 2015a). With our measurements of the average spectral properties of the *NuSTAR* sources we find that the typical contribution from Compton reflection in the spectra is relatively small, and although values up to  $R \approx 2$  are found for the low-luminosity AGNs (see Figure 11), these constitute a small fraction of the population probed by *NuSTAR*, especially at  $z > 0.5$ . Therefore, our results seem to support the Aird et al. (2015b) model over the Ueda et al. (2014) model, under the assumptions made in Aird et al. (2015a).

## 7. Summary

Constructing the rest-frame composite spectra for all the *NuSTAR*-detected AGNs in the E-CDFS, EGS, and COSMOS fields, using *Chandra* and *NuSTAR* data, we have investigated the average spectral properties of the BL and NL AGNs, as

well as those of the HB- and SB-detected sources; we also studied the spectral properties as a function of X-ray absorption ( $N_{\text{H}}$ ) and of X-ray luminosity at 10–40 keV, producing and analyzing the composite spectra in three different  $N_{\text{H}}$  bins and  $L_{10-40 \text{ keV}}$  bins. With this work we find the following:

1. The average broad X-ray band (2–40 keV, rest frame) spectral slope for BL AGNs and unabsorbed sources is  $\Gamma \approx 1.8$ , consistent with previous results at similar energy ranges (Burlon et al. 2011; Ricci et al. 2011; Alexander et al. 2013); while for NL AGNs and X-ray absorbed sources we typically find flatter  $\Gamma \approx 1.4-1.6$ , likely due to the effects of absorption and the contribution of Compton reflection at high energies (Sections 4.1 and 4.3).
2. The average reflection fraction ( $R$ ) found in our spectra is  $R \approx 0.5$  for typical  $\Gamma = 1.8$ . Assuming the same intrinsic spectral slope for all the sources, to avoid parameter degeneracy, NL AGNs and absorbed sources tend to have higher  $R$  values ( $R \approx 0.5-0.7$ ) compared to the BL and unabsorbed AGNs ( $R \lesssim 0.2$ ; see also Figure 10, left panel). However, better counting statistics in the most heavily obscured AGN spectra are needed to assess whether there is any real correlation between  $R$  and  $N_{\text{H}}$  (Sections 4.1 and 4.3).
3. We find that the reflection strength for low-luminosity AGNs ( $L_{10-40 \text{ keV}} < 10^{44} \text{ erg s}^{-1}$ ) is relatively high ( $R \approx 1.2$ ) and decreases at high luminosities ( $L_{10-40 \text{ keV}} > 10^{44} \text{ erg s}^{-1}$ ), for which  $R \approx 0.3$  (Section 4.4), as found in some previous studies (e.g., Bianchi et al. 2007; Liu et al. 2016). Although we cannot establish a statistically significant correlation, due to the small number of data points and their uncertainties, this decreasing trend of  $R$  with luminosity is seen at all assumed  $\Gamma$  (Section 6), and it seems to be present also in dividing the high- and low-luminosity sources into obscured and unobscured (see Section 4.5).
4. We find that the EW of the iron  $K\alpha$  line has a similar dependence on  $N_{\text{H}}$  and luminosity to that seen for the reflection strength, as would be expected, since they are supposed to originate from the same reflecting material in the nuclear region. In particular, the EW seems to decrease with the X-ray luminosity. With the current data, the anticorrelation is not statistically significant, due to the large uncertainties; however, the trend is consistent with the X-ray Baldwin effect (see Section 4.4), found in previous works (e.g., Iwasawa & Taniguchi 1993; Nandra et al. 1997; Page et al. 2004; Bianchi et al. 2007; Ricci et al. 2013a).
5. Our results are in line with the assumptions made in the Gilli et al. (2007) CXB model for the intrinsic AGN spectra; however, there are some differences, also comparing to other CXB models (e.g., Ueda et al. 2003; Ballantyne et al. 2006; Treister et al. 2009; Ueda et al. 2014). Detailed modeling, with our improved  $R$  estimates, is needed to reliably assess whether our results have a significant impact on the CXB model results, e.g., on the CT AGN fraction needed to reproduce the CXB peak (e.g., Treister et al. 2009; Akylas et al. 2012).
6. From the simple spectral fitting of individual sources we identify five CT AGN candidates, which have hydrogen column density values in the CT range, within the errors. The joint spectral fitting of these sources with more complex, physical models (see Section 5) provides

solutions consistent with a CT interpretation. However, a strong Fe  $K\alpha$  emission line, which is a typical feature in CT AGNs (EW  $\sim 1$  keV), could not be constrained in the fit (EW  $< 0.7$  keV from the joint-fitting results), and it is not possible to confirm the CT nature of these sources individually with the current data (except for *NuSTAR* ID 330; see Civano et al. 2015).

Further improvement on the constraints found in our work will likely be provided by the large AGN samples yielded by the *NuSTAR* Serendipitous survey (Lansbury et al. 2017). These sources have been excluded from our analyses owing to the heterogeneity of the lower energy coverage, which would increase the systematic errors in our composite spectra. However, larger numbers of sources are needed to reduce the scatter on the composite spectra and therefore place tighter constraints on the average spectral parameters. Moreover, deeper *NuSTAR* observations on the current survey fields would also be helpful to increase the S/N of the individual spectra; this would allow us to perform detailed analyses of the individual sources and thus provide important constraints on the distribution of the spectral parameters ( $\Gamma$ ,  $N_{\text{H}}$ , and  $R$ ).

We thank A. Corral for useful discussions about the spectral averaging method presented in her work. A.D.M. thanks the financial support from the Max Planck Society and the UK Science and Technology Facilities Council (STFC, ST/L00075X/1, A.D.M. and D.M.A.; ST/K501979/1, G.B.L.). F.E.B. and E.T. acknowledge support from CONICYT-Chile (Basal-CATA PFB-06/2007, “EMBIGGEN” Anillo ACT1101, FONDECYT Regular 1141218 [F.E.B.] and 1160999 [E.T.]); F.E.B. also thanks the Ministry of Economy, Development, and Tourism’s Millennium Science Initiative through grant IC120009, awarded to the Millennium Institute of Astrophysics (MAS). P.G. thanks the STFC for support (ST/J003697/2). W.N.B. acknowledges support from the Caltech *NuSTAR* subcontract 44A-1092750 and NASA ADP grant NNX10AC99G. A.C. and L.Z. acknowledge support from the ASI/INAF grant I/037/12/0 011/13.

This work was supported under NASA contract no. NNG08FD60C and made use of data from the *NuSTAR* mission, a project led by the California Institute of Technology, managed by the Jet Propulsion Laboratory, and funded by the National Aeronautics and Space Administration. We thank the *NuSTAR* Operations, Software, and Calibration teams for support with the execution and analysis of these observations. This research has made use of the *NuSTAR* Data Analysis Software (NuSTARDAS) jointly developed by the ASI Science Data Center (ASDC, Italy) and the California Institute of Technology (USA).

## Appendix Spectral Simulations

To test the results obtained from our spectral stacking procedure and to understand the effects and distortions that might be introduced at various stages of the process, we performed extensive spectral simulations. These are essential to understanding the intrinsic spectral properties derived from the average spectra. We therefore performed various tests, simulating *NuSTAR* and *Chandra* spectra with (i) a range of photon indices ( $\Gamma = 1.6-2.0$ ) and (ii) a fixed photon index

( $\Gamma = 1.8$ ) and various levels of column densities, and running the same stacking procedure used for the real data.

### A.1. Combining Spectra with Different Spectral Slopes

We initially simulated *NuSTAR* and *Chandra* spectra as a simple power law with  $\Gamma = 1.8$  fixed, using the response and ancillary files extracted from our survey data and a flux distribution similar to that of the real sources. For practicality, since the simulations are very time-consuming, we only used the files of the sources detected in the E-CDFS field to simulate the spectra (i.e., 45 sources). When more spectra are needed to increase the counting statistics in the composite spectra (see below), we generated multiple simulated spectra for each real source (using photon randomization). We simulated both background and source spectra to test more closely the results from the real data. We applied to the simulated spectra the same procedure used for the real data (see Section 3.2), i.e., we fitted the individual background-subtracted spectra with a power-law model (with  $\Gamma$  free to vary) and saved them in physical units (unfolded spectrum in XSPEC); shifted the spectra to the rest frame, using the redshifts of our real sources; created a new energy grid for all the spectra; normalized them to the flux at 8–15 keV; and redistributed the fluxes in the new energy bins. Our average spectra are obtained by taking the median flux in each new energy bin, performing a resampling analysis to estimate the  $1\sigma$  errors. We then fitted the obtained spectrum with a power-law model to verify whether we can recover the input photon index of the simulated spectra. We obtained  $\Gamma = 1.77 \pm 0.03$ , which is slightly lower than the input spectral slope, but in good agreement, within the errors, with the input parameters.

We performed the same test simulating spectra with different photon indices (45 spectra for each  $\Gamma$  value), in the range of  $\Gamma = 1.6$ –2.0, with a step size of  $\Delta\Gamma = 0.5$  and obtaining the average spectrum for each input spectral slope. Subsequently, we also combined spectra with different slopes, to test whether we can recover the median input  $\Gamma$  from our composite spectra or whether significant distortions are affecting the spectra. In Figure 12 we show the results of these tests by plotting the resulting spectral slopes, obtained by fitting the composite spectra with a power-law model, versus the input  $\Gamma$  used to simulate the individual spectra. When spectra with different slopes are combined, we plot their median  $\Gamma$  on the  $x$ -axis. In general, the spectral slopes obtained from the composite spectra are in good agreement with the input  $\Gamma$  of the simulated spectra used to produce the composites. However, for steep slopes ( $\Gamma > 1.9$ ), the resulting  $\Gamma$  tends to be flatter than the input values. This is likely because when the spectra are steep, there are fewer counts contributing to the spectra at high energies (e.g., in the *NuSTAR* band), increasing the scatter in the composite spectra at  $E \gtrsim 10$  keV, thus impairing the constraints on the intrinsic spectral slope. This results in a slightly flatter value of  $\Gamma$ . We note that this issue is affecting the results only when a relatively small number of spectra are used to produce the composites (for instance, 45 spectra in our tests with single  $\Gamma$  values), while when we increase the number of spectra (hence, the counting statistics), as in the case of the composites obtained from spectra with different  $\Gamma$  values, the issue is no longer present.

We can therefore conclude that our averaging method does not introduce significant distortions to the final composite spectra when combining spectra with different slopes, in the

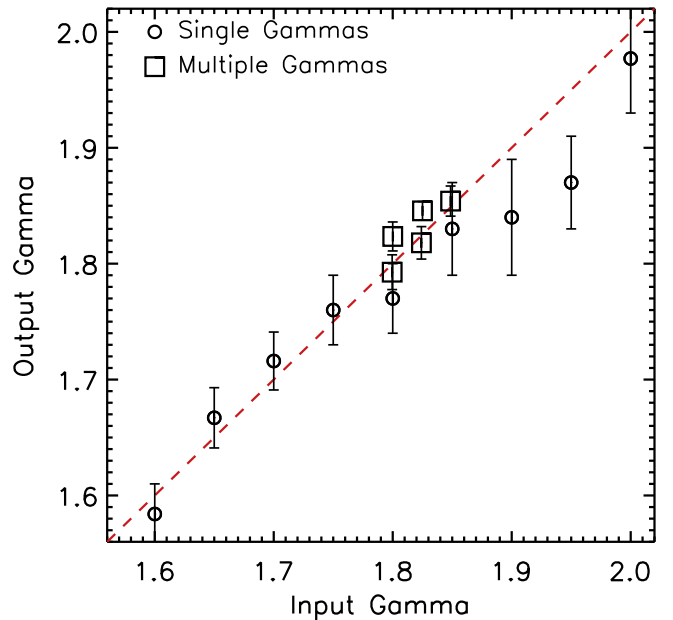


**Figure 12.** Spectral slopes (output  $\Gamma$ ) obtained from the composite spectra produced using simulated *NuSTAR*+*Chandra* spectra with different spectral slopes (input  $\Gamma$ ) in the range between 1.6 and 2.0. The circles represent the results from the composite spectra obtained combining spectra with one single value of  $\Gamma$  (typically  $\sim 45$  simulated spectra for each composite), while the squares represent the results obtained combining spectra with different slopes (typically  $> 90$  simulated spectra for each composite); in these cases we plot the median of the input  $\Gamma$  distribution on the  $x$ -axis. The red dashed line represents the 1:1 line.

case where a simple power-law model is assumed. From our tests on these simulated composite spectra we can reliably recover the input  $\Gamma$  of the individual spectra, and/or their median value, when a distribution of  $\Gamma$  is assumed.

### A.2. Simulations with Various Column Densities: The Effects of Absorption

An important effect that can create distortions in the composite spectra and modify the results from our analyses is the X-ray column density. To test how the X-ray absorption modifies the composite spectra, we simulated the *Chandra* and *NuSTAR* source spectra (and the relative background) with different values of  $N_{\text{H}}$  ( $N_{\text{H}} = 10^{21}, 10^{22}, 10^{23}, 5 \times 10^{23} \text{ cm}^{-2}$ ) and a fixed  $\Gamma = 1.8$  and produced the composite rest-frame spectra for individual values of  $N_{\text{H}}$ . An example is shown in Figure 13. Analyzing the spectra (at  $E \approx 3$ –30 keV, rest frame), in all cases we obtained parameters in good agreement with the input values; the results are summarized in Table 4. We note that for the  $N_{\text{H}} = 10^{21} \text{ cm}^{-2}$  composite, where we obtained a much lower  $N_{\text{H}}$  value than the input simulated spectra, the discrepancy is due to the fact that we cannot constrain such a low value of  $N_{\text{H}}$  from our composite spectrum, as it spans the energy range  $E \approx 3$ –40 keV, rest frame. For high levels of  $N_{\text{H}}$  the resulting photon index tends to be slightly flatter than the input  $\Gamma = 1.8$ , but it is always consistent within the errors. In these cases, the flattening is likely due to a decrease of the number of counts in the composite spectra at low energies, due to the absorption, thus yielding poorer constraints on the intrinsic spectral slope.

We then produced composite spectra combining simulated source spectra with different levels of absorption, to see

**Table 4**  
Spectral Parameters of the Simulated Composite Spectra, Obtained Combining Simulated *Chandra*+*NuSTAR* Spectra with  $\Gamma = 1.8$  and Different Levels of X-ray Absorption

Input $N_{\text{H}}^{\text{a}}$	No. of Sources	$\Gamma$	$N_{\text{H}}^{\text{a}}$
0.1	45	$1.83 \pm 0.01$	$<0.05$
1.0	45	$1.82 \pm 0.02$	$0.9 \pm 0.1$
10.0	45	$1.78 \pm 0.02$	$10.1 \pm 0.2$
50.0	45	$1.75 \pm 0.07$	$51.4 \pm 2.7$
0.1, 1.0 (a)	90	$1.79 \pm 0.03$	$0.6 \pm 0.1$
1.0, 10.0 (b)	90 (180)	$1.72 \pm 0.05$ ( $1.78 \pm 0.03$ )	$6.3 \pm 0.7$ ( $6.3 \pm 0.4$ )
0.1, 1.0, 10.0 (c)	135	$1.76 \pm 0.04$	$4.0 \pm 0.7$

**Note.**

<sup>a</sup> The hydrogen column density is expressed in units of  $10^{22} \text{ cm}^{-2}$ .

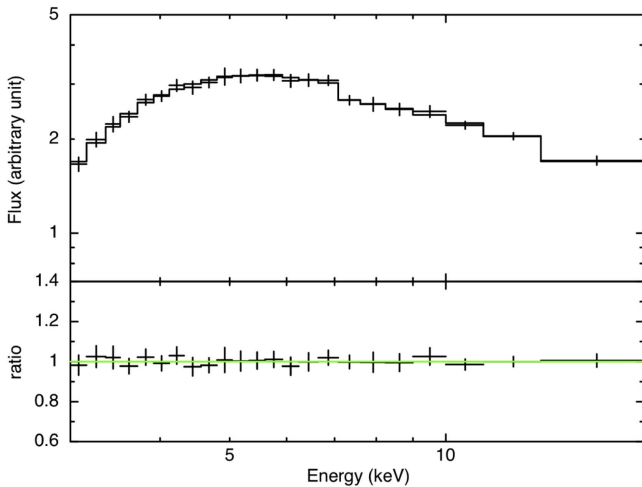


**Figure 13.** Median rest-frame spectrum from the simulated *Chandra* and *NuSTAR* spectra with  $\Gamma = 1.8$  and  $N_{\text{H}} = 10^{23} \text{ cm}^{-2}$ . To test the reliability of our averaging method and constrain the underlying continuum, the median spectrum was fitted with an absorbed power-law model between 3 and 30 keV: we recovered the input photon index  $\Gamma = 1.8$  and  $N_{\text{H}} = 10^{23} \text{ cm}^{-2}$  with a scatter of  $\sim 1\%$  and  $\sim 2\%$ , respectively. The bottom panel shows the ratio between the simulated data and the model.

whether, also in these cases, the resulting spectral parameters are in agreement with the input distributions. We note that we do not expect to obtain the true median value of  $N_{\text{H}}$  from the composite spectra, as the absorption is not a linear parameter. However, the resulting  $N_{\text{H}}$  should be somewhat consistent with (or within the range of) the input values. We therefore combined spectra with (a)  $N_{\text{H}} = 10^{21}, 10^{22} \text{ cm}^{-2}$ ; (b)  $N_{\text{H}} = 10^{22}, 10^{23} \text{ cm}^{-2}$ ; and (c)  $N_{\text{H}} = 10^{21}, 10^{22}, 10^{23} \text{ cm}^{-2}$ . The spectral parameters obtained from these composite spectra are reported in Table 4. For the unabsorbed and lightly absorbed sources (composite spectrum “a”) the resulting parameters are in very good agreement with those of the input simulated spectra, while for spectra “b” and “c,” which also include more absorbed sources, the resulting spectral slope tends to be flatter than those of the input sources. The flattening is mainly due, as described above, to a decrease of the number of counts in the composite spectra for the absorbed sources. Indeed, we tested that increasing the number of input spectra to produce the composite “b” (e.g., from 90 to 180; see Table 4), thus, increasing the counting statistics in the composite spectrum, we can recover a photon index in good agreement with the  $\Gamma = 1.8$  of the input spectra. However, another effect

plays a non-negligible role in flattening the photon index of the composite spectra: combining spectra with different values of column densities, and therefore different photoelectric cutoff energies, can lead to a slight flattening in the spectral slope, as the typical absorption features get “smoothed” in the final composites, yielding a flatter  $\Gamma$  and possibly an underestimation of  $N_{\text{H}}$  (since it is not possible to recover the true median value of  $N_{\text{H}}$  from the composite spectra). This effect is also seen in the real data (Sections 4.1 and 4.3 and Figure 5). However, our simulations indicate that this “artificial” flattening of the spectra due to the averaging process is relatively small ( $\Delta\Gamma \approx 0.2\text{--}0.8$ ) and cannot be the sole cause of the flat spectral slopes seen in the composites of the NL AGNs and the heavily absorbed sources (NH3), for which the resulting photon indices are  $\Gamma \approx 1.6$ .

### A.3. Arithmetic Mean, Geometric Mean, and Median

There are different methods one can use to determine the average spectrum of a population. The arithmetic mean (or median) tends to preserve the relative fluxes of the emission features, while the geometric mean tends to preserve the global continuum shape, when it can be approximated by a power law (Vanden Berk et al. 2001). Since the aim of our analyses is to study the intrinsic AGN continuum, the geometric mean would be the most appropriate choice to derive our composite spectra. However, since the *NuSTAR* spectra have typically high background levels, several energy bins in the individual spectra result in a null (or negative) flux value after background subtraction, due to the background fluctuations. These energy bins have to be excluded from the geometric mean, therefore biasing the resulting average flux.

We performed several tests to assess the differences between these averaging methods and evaluate the best approach to use for our data. We initially used the simulated spectra (see details in the previous section) with known input spectral slopes and analyzed the resulting composite spectra. When we produce composite spectra for unabsorbed  $\Gamma = 1.8$  simulated spectra, the three averaging methods yield comparable results, recovering the input  $\Gamma = 1.8$ . When we introduce various levels of absorption in our simulated spectra, however, the resulting composite spectra are affected by some distortions (see details below), and the averaging methods used to produce the composite spectra yield different results. In Figure 14 we show the confidence contours for the spectral parameters  $\Gamma$  and  $N_{\text{H}}$  derived from the composite spectra. On the left the input spectra used for the composite are all simulated with the same  $\Gamma = 1.8$  and  $N_{\text{H}} = 10^{23} \text{ cm}^{-2}$  (which are the values we want to

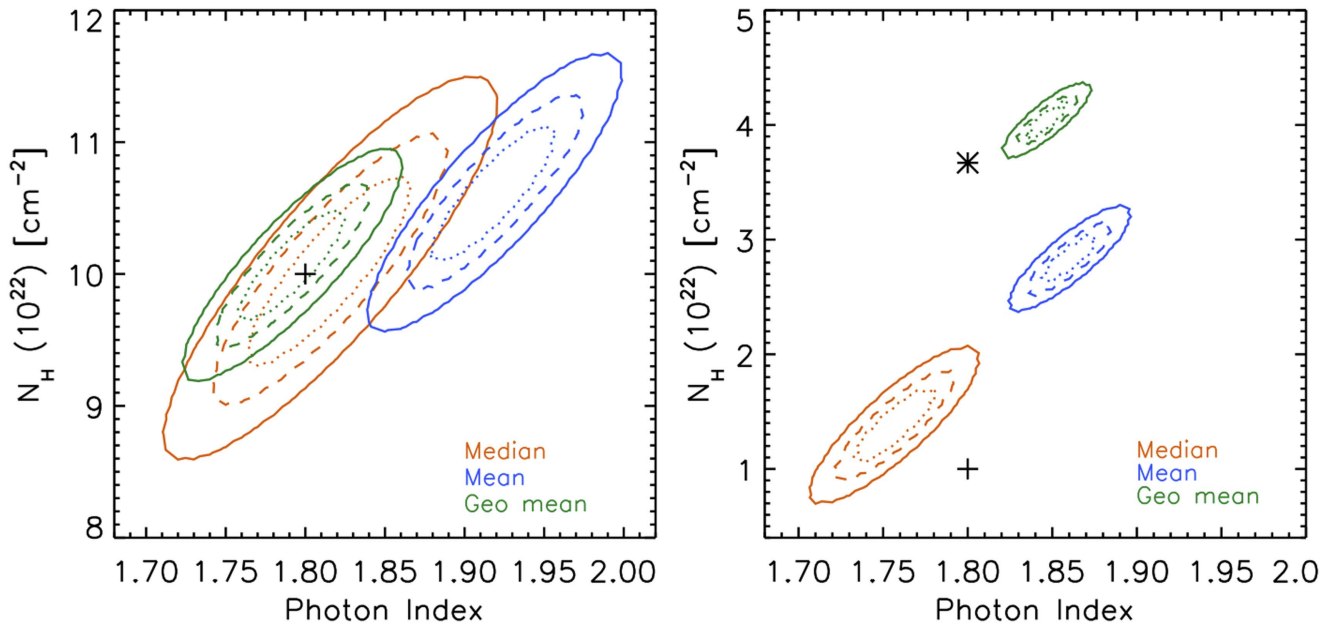


**Figure 14.** Confidence contours for the spectral parameters  $\Gamma$  and  $N_{\text{H}}$  recovered from the composite simulated spectra, with input  $\Gamma = 1.8$  and  $N_{\text{H}} = 10^{23} \text{ cm}^{-2}$  (left) and  $\Gamma = 1.8$  and  $N_{\text{H}} = 0, 10^{22}, 10^{23} \text{ cm}^{-2}$  (right), using the arithmetic mean (blue), median (orange), and geometric mean (green) as averaging methods. The contours correspond to 68%, 90%, and 99% confidence levels (dotted, dashed, and solid curves, respectively). The black cross marks the median of the input parameters, and the asterisk marks the mean values.

recover from the resulting composite spectra); on the right the input spectra used for the composite have a photon index  $\Gamma = 1.8$  and  $N_{\text{H}} = 0, 10^{22}, 10^{23} \text{ cm}^{-2}$  in equal numbers. The median and the geometric mean provide comparable results in the first case, while the arithmetic mean yields a steeper photon index than the input value. When spectra with various column densities are stacked together to produce the composite, the parameters derived from the median spectrum are consistent with the input  $N_{\text{H}}$  values of the individual spectra (although we do not expect to recover the true median  $N_{\text{H}}$ , as described in the previous section), while slightly underestimating the photon index, which is flatter than the input value  $\Gamma = 1.8$ , but still consistent within the errors. On the other hand,  $\Gamma$  tends to be overestimated in the composite generated adopting the geometric mean, as well as the arithmetic mean. We also note that, since the median is less sensitive to outliers or extreme values, the composite spectrum produced with this method is less noisy than those produced using the arithmetic or geometric means. We therefore favor the median as the method to produce our composite spectra (see also Falocco et al. 2012), keeping in mind that the flattening of the photon index seen in the composite spectra of our real data is partially due to the stacking method (see previous section).

#### ORCID iDs

D. M. Alexander <https://orcid.org/0000-0002-5896-6313>  
 J. A. Aird <https://orcid.org/0000-0003-1908-8463>  
 F. E. Bauer <https://orcid.org/0000-0002-8686-8737>  
 J. R. Mullaney <https://orcid.org/0000-0002-3126-6712>  
 D. R. Ballantyne <https://orcid.org/0000-0001-8128-6976>  
 W. N. Brandt <https://orcid.org/0000-0002-0167-2453>  
 A. Comastri <https://orcid.org/0000-0003-3451-9970>  
 P. Gandhi <https://orcid.org/0000-0003-3105-2615>  
 F. A. Harrison <https://orcid.org/0000-0003-2992-8024>  
 G. B. Lansbury <https://orcid.org/0000-0002-5328-9827>  
 L. Lanz <https://orcid.org/0000-0002-3249-8224>

B. Luo <https://orcid.org/0000-0002-9036-0063>  
 S. Marchesi <https://orcid.org/0000-0001-5544-0749>  
 S. Puccetti <https://orcid.org/0000-0002-2734-7835>  
 C. Ricci <https://orcid.org/0000-0001-5231-2645>  
 D. Stern <https://orcid.org/0000-0003-2686-9241>

#### References

- Aird, J., Alexander, D. M., Ballantyne, D. R., et al. 2015a, *ApJ*, **815**, 66  
 Aird, J., Coil, A. L., Georgakakis, A., et al. 2015b, *MNRAS*, **451**, 1892  
 Ajello, M., Greiner, J., Sato, G., et al. 2008, *ApJ*, **689**, 666  
 Akylas, A., Georgakakis, A., Georgantopoulos, I., Brightman, M., & Nandra, K. 2012, *A&A*, **546**, A98  
 Alexander, D. M., Stern, D., Del Moro, A., et al. 2013, *ApJ*, **773**, 125  
 Ballantyne, D. R. 2009, *ApJ*, **698**, 1033  
 Ballantyne, D. R. 2014, *MNRAS*, **437**, 2845  
 Ballantyne, D. R., Draper, A. R., Madsen, K. K., Rigby, J. R., & Treister, E. 2011, *ApJ*, **736**, 56  
 Ballantyne, D. R., Everett, J. E., & Murray, N. 2006, *ApJ*, **639**, 740  
 Bianchi, S., Bonilla, N. F., Guainazzi, M., Matt, G., & Ponti, G. 2009, *A&A*, **501**, 915  
 Bianchi, S., Guainazzi, M., Matt, G., & Fonseca Bonilla, N. 2007, *A&A*, **467**, L19  
 Bottacini, E., Ajello, M., & Greiner, J. 2012, *ApJS*, **201**, 34  
 Brightman, M., & Nandra, K. 2011, *MNRAS*, **413**, 1206  
 Brightman, M., Nandra, K., Salvato, M., et al. 2014, *MNRAS*, **443**, 1999  
 Brightman, M., Silverman, J. D., Mainieri, V., et al. 2013, *MNRAS*, **433**, 2485  
 Broos, P., Townsley, L., Getman, K., & Bauer, F. 2012, AE: ACIS Extract, Astrophysics Source Code Library, ascl:1203.001  
 Broos, P. S., Townsley, L. K., Feigelson, E. D., et al. 2010, *ApJ*, **714**, 1582  
 Brusa, M., Civano, F., Comastri, A., et al. 2010, *ApJ*, **716**, 348  
 Burlon, D., Ajello, M., Greiner, J., et al. 2011, *ApJ*, **728**, 58  
 Caccianiga, A., Severgnini, P., Braito, V., et al. 2004, *A&A*, **416**, 901  
 Cash, W. 1979, *ApJ*, **228**, 939  
 Civano, F., Hickox, R. C., Puccetti, S., et al. 2015, *ApJ*, **808**, 185  
 Civano, F., Marchesi, S., Comastri, A., et al. 2016, *ApJ*, **819**, 62  
 Comastri, A., Setti, G., Zamorani, G., & Hasinger, G. 1995, *A&A*, **296**, 1  
 Corral, A., Della Ceca, R., Caccianiga, A., et al. 2011, *A&A*, **530**, A42  
 Corral, A., Page, M. J., Carrera, F. J., et al. 2008, *A&A*, **492**, 71  
 Dai, X., Chartas, G., Eracleous, M., & Garmire, G. P. 2004, *ApJ*, **605**, 45  
 Del Moro, A., Alexander, D. M., Bauer, F. E., et al. 2016, *MNRAS*, **456**, 2105  
 Del Moro, A., Mullaney, J. R., Alexander, D. M., et al. 2014, *ApJ*, **786**, 16  
 Dickey, J. M., & Lockman, F. J. 1990, *ARA&A*, **28**, 215

- Elvis, M., Civano, F., Vignali, C., et al. 2009, *ApJS*, 184, 158
- Esposito, V., & Walter, R. 2016, *A&A*, 590, A49
- Falocco, S., Carrera, F. J., Corral, A., et al. 2012, *A&A*, 538, A83
- Falocco, S., Carrera, F. J., Corral, A., et al. 2013, *A&A*, 555, A79
- Gandhi, P., Annuar, A., Lansbury, G. B., et al. 2017, *MNRAS*, 467, 4606
- Gandhi, P., Fabian, A. C., Suebawong, T., et al. 2007, *MNRAS*, 382, 1005
- Gilli, R., Comastri, A., & Hasinger, G. 2007, *A&A*, 463, 79
- Harrison, F. A., Aird, J., Civano, F., et al. 2016, *ApJ*, 831, 185
- Harrison, F. A., Craig, W. W., Christensen, F. E., et al. 2013, *ApJ*, 770, 103
- Hickox, R. C., & Markevitch, M. 2006, *ApJ*, 645, 95
- Iwasawa, K., Gilli, R., Vignali, C., et al. 2012, *A&A*, 546, A84
- Iwasawa, K., & Taniguchi, Y. 1993, *ApJL*, 413, L15
- Krivonos, R., Revnivtsev, M., Lutovinov, A., et al. 2007, *A&A*, 475, 775
- Lansbury, G. B., Alexander, D. M., Del Moro, A., et al. 2014, *ApJ*, 785, 17
- Lansbury, G. B., Gandhi, P., Alexander, D. M., et al. 2015, *ApJ*, 809, 115
- Lansbury, G. B., Stern, D., Aird, J., et al. 2017, *ApJ*, 836, 99
- Lanzuisi, G., Ranalli, P., Georgantopoulos, I., et al. 2015, *A&A*, 573, A137
- Lehmer, B. D., Brandt, W. N., Alexander, D. M., et al. 2005, *ApJS*, 161, 21
- Liu, Z., Merloni, A., Georgakakis, A., et al. 2016, *MNRAS*, 459, 1602
- Madsen, K. K., Harrison, F. A., Markwardt, C. B., et al. 2015, *ApJS*, 220, 8
- Magdziarz, P., & Zdziarski, A. A. 1995, *MNRAS*, 273, 837
- Mainieri, V., Bergeron, J., Hasinger, G., et al. 2002, *A&A*, 393, 425
- Marchesi, S., Civano, F., Elvis, M., et al. 2016, *ApJ*, 817, 34
- Mateos, S., Barcons, X., Carrera, F. J., et al. 2005, *A&A*, 433, 855
- Molina, M., Bassani, L., Malizia, A., et al. 2009, *MNRAS*, 399, 1293
- Mullaney, J. R., Del-Moro, A., Aird, J., et al. 2015, *ApJ*, 808, 184
- Murphy, E. J., Chary, R.-R., Alexander, D. M., et al. 2009, *ApJ*, 698, 1380
- Nandra, K., George, I. M., Mushotzky, R. F., Turner, T. J., & Yaqoob, T. 1997, *ApJL*, 488, L91
- Nandra, K., Laird, E. S., Aird, J. A., et al. 2015, *ApJS*, 220, 10
- Nandra, K., & Pounds, K. A. 1994, *MNRAS*, 268, 405
- Page, K. L., O'Brien, P. T., Reeves, J. N., & Turner, M. J. L. 2004, *MNRAS*, 347, 316
- Politis, D. N., & Romano, J. P. 1994, *AnSta*, 22, 2031
- Ranalli, P., Comastri, A., Vignali, C., et al. 2013, *A&A*, 555, A42
- Ricci, C., Paltani, S., Awaki, H., et al. 2013a, *A&A*, 553, A29
- Ricci, C., Paltani, S., Ueda, Y., & Awaki, H. 2013b, *MNRAS*, 435, 1840
- Ricci, C., Walter, R., Courvoisier, T. J.-L., & Paltani, S. 2011, *A&A*, 532, A102
- Ross, R. R., & Fabian, A. C. 2005, *MNRAS*, 358, 211
- Saez, C., Chartas, G., Brandt, W. N., et al. 2008, *AJ*, 135, 1505
- Scott, A. E., Stewart, G. C., Mateos, S., et al. 2011, *MNRAS*, 417, 992
- Shu, X. W., Yaqoob, T., & Wang, J. X. 2010, *ApJS*, 187, 581
- Spergel, D. N., Verde, L., Peiris, H. V., et al. 2003, *ApJS*, 148, 175
- Tozzi, P., Gilli, R., Mainieri, V., et al. 2006, *A&A*, 451, 457
- Treister, E., & Urry, C. M. 2005, *ApJ*, 630, 115
- Treister, E., Urry, C. M., & Virani, S. 2009, *ApJ*, 696, 110
- Ueda, Y., Akiyama, M., Hasinger, G., Miyaji, T., & Watson, M. G. 2014, *ApJ*, 786, 104
- Ueda, Y., Akiyama, M., Ohta, K., & Miyaji, T. 2003, *ApJ*, 598, 886
- Vanden Berk, D. E., Richards, G. T., Bauer, A., et al. 2001, *AJ*, 122, 549
- Vasudevan, R. V., Mushotzky, R. F., & Gandhi, P. 2013, *ApJL*, 770, L37
- Vignali, C., Iwasawa, K., Comastri, A., et al. 2015, *A&A*, 583, A141
- Winter, L. M., Mushotzky, R. F., Reynolds, C. S., & Tueller, J. 2009, *ApJ*, 690, 1322
- Xue, Y. Q., Luo, B., Brandt, W. N., et al. 2011, *ApJS*, 195, 10
- Xue, Y. Q., Luo, B., Brandt, W. N., et al. 2016, *ApJS*, 224, 15
- Xue, Y. Q., Wang, S. X., Brandt, W. N., et al. 2012, *ApJ*, 758, 129
- Yaqoob, T. 2007, in ASP Conf. Ser. 373, The Central Engine of Active Galactic Nuclei, ed. L. C. Ho & J.-W. Wang (San Francisco, CA: ASP), 109